Unraveling the role of cobalt in the direct conversion of CO_2 to high-yield liquid fuels and lube base oil

Heuntae Jo [a], Muhammad Kashif Khan [a,b], Muhammad Irshad [b], Malik Waqar Arshad [c,d], Seok Ki Kim [c,*], Jaehoon Kim [a,b,e,**]

[a] School of Mechanical Engineering, Sungkyunkwan University, 2066, Seobu-Ro, Jangan-Gu, Suwon, Gyeong Gi-Do 16419, South Korea
[b] School of Chemical Engineering, Sungkyunkwan University, 2066, Seobu-Ro, Jangan-Gu, Suwon, Gyeong Gi-Do 16419, South Korea
[c] Carbon Resource Institute, Korea Research Institute of Chemical Technology, 141 Gajeongro, Yuseong, Daejeon 34114, South Korea
[d] University of Science and Technology, Advanced Materials and Chemical Engineering Technology, 217 Gajeong-ro, Yuseong-gu, Daejeon 34113, South Korea
[e] SKKU Advanced Institute of Nano Technology, 2066, Seobu-Ro, Jangan-Gu, Suwon, Gyeong Gi-Do 16419, South Korea

ARTICLE INFO

ABSTRACT

Owing to their high CO_2 methanation activity, the direct hydrogenation of CO_2 to long-chain C_{5+} over Co-based catalysts is challenging. Here, we demonstrate a Na- and Mn-promoted, core-shell $Co@CoO_x/Co_2C$ catalyst that produces a high C_{5+} yield of 21.1% at a CO_2 conversion of 64.3% and low temperature of 270 °C. CO_2 conversion and C_{5+} selectivity are ensured during long-term catalytic reactions up to 1425 h. C_{21+} selectivity increases to 14.9% with increasing time on stream. The catalyst exhibits high C_{5+} and C_{21+} selectivity, making it a promising option for producing liquid fuels and lube base oil in one-pass CO_2 conversion. Direct CO_2 dissociation and formate formation over the oxygen-vacant Co_3O_4 phase in the shell is the plausible reverse–water–gas–shift reaction mechanism. The Mn promoter facilitates the formation of the CoO_x phase at the outermost surface, suppressing the direct contact between CO_2 and the metallic Co core.

1. Introduction

The development of effective CO_2 utilization techniques for producing fuels and chemicals is a highly promising strategy for establishing a CO_2-neutral and sustainable society. The thermocatalytic conversion of CO_2, which is primarily based on reverse–water–gas–shift (RWGS) and subsequent Fischer–Tropsch synthesis (FTS), is considered a promising approach for producing gas fuels (C_1–C_4), liquid fuels (C_{5+}), and value-added platform chemicals (e.g., olefins, acids, alcohols, and aromatics) [1–4]. Iron-based and cobalt-based catalysts, which are the most frequently exploited FTS catalysts used for the conversion of syngas (H_2/CO mixture) to alkanes, alkenes, and oxygenates, have been adopted for direct CO_2 hydrogenation [1]. An Fe-based catalyst exhibits similar catalytic performance regardless of whether CO or CO_2 is used as the feed [5,6]; when this catalyst is used, the RWGS reaction of CO_2 over the Fe_3O_4 site is promoted via a redox cycle, and subsequent FTS over an Fe_5C_2 site can result in high-yield C_{5+} (up to approximately 20% at a gas hour space velocity (GHSV) $\geq$ 4000 mL g^{-1} h^{-1}, Table S1). Co-based

catalysts are highly efficient in the FTS of syngas, which is used for producing long-chain hydrocarbons at relatively low temperatures (<240 °C), owing to characteristics such as their high chain growth probability (up to 0.94), high turnover rates, high selectivity to linear paraffins, low WGS reaction activity, high deactivation resistance to water molecules that form during FTS, and high long-term stability [7]. A metallic Co center is considered the major active site for CO hydrogenation when producing long-chain hydrocarbons under typical FTS conditions [7]. Recently, the possible activation of CO over a Co_2C phase when producing lower olefins was suggested [8]. However, in case of direct CO_2 hydrogenation over Co-based catalysts, the dominant product is CH_4, and the C_{5+} yields are very low (<5% at GHSV $\geq$ 4000 mL g^{-1} h^{-1}, Table S1). The high tendency of the Co-based catalysts toward CO_2 methanation is attributed to the absence of active sites that can facilitate RWGS to establish a sufficient FTS regime [5,9] and the low C/H ratio on the active surface that favors the hydrogenation of CO_2-adsorbed species rather than the chain-extension reaction[10]. Bimetallic CoFe [11] and CoNi [12] catalysts have been proposed to directly convert CO_2 to light

---

olefins and ethanol, respectively. However, a lack of fundamental and comprehensive understanding of active sites for synthesizing long-chain hydrocarbons directly from CO_2 makes it difficult to design potential Co-based catalysts.

In this study, we demonstrated that a core-shell $Co@CoO_x/Co_2C$ catalyst promoted with Na and manganese oxide is highly efficient in producing C_{5+} via direct CO_2 hydrogenation. The Na-promoted $Co@CoO_x/Co_2C$ catalyst with Mn/[Co+Mn] = 0.1 exhibited a high C_{5+} yield of 21.1% (including CO) at a CO_2 conversion of 64.3% at a low temperature of 270 °C, pressure of 4.0 MPa, H_2/CO_2 = 3:1, and GHSV of 4000 mL g^{-1} h^{-1}. This C_{5+} yield exceeds values predicted using the Anderson–Schulz–Flory distribution model of the previous Co-based catalysts in the CO_2 conversion [13]. The C_{5+} yield produced over the Mn-promoted $Co@CoO_x/Co_2C$ catalyst was significantly higher than that over previously reported Co-based catalysts (Tables S1 and S2, Fig. S1). Meanwhile, the production of CO was highly suppressed (0.2% selectivity). The catalyst was stable for up to 1425 h on the stream and maintained CO_2 conversion and C_{5+} selectivity. The selectivity toward C_{21+}, which is lube oil fraction, increases to 14.9% with increasing time on stream. Therefore, the unique features of Co-based catalysts in both CO (low-temperature reaction, high C_{5+} selectivity, and high stability) and CO_2 (high CO_2 conversion, low CO selectivity) hydrogenation can be achieved using this single $Co@CoO_x/Co_2C$ catalyst without the need for additional C–C coupling agents (e.g., zeolites).

2. Experimental section

2.1. Catalyst synthesis

The Na- and Mn-promoted core-shell $Co@CoO_x/Co_2C$ catalysts (CMO-*y*, where *y* indicates the mol% of Mn) were synthesized using a co-precipitation method. Experimentally desired amounts of cobalt nitrate $(Co(NO_3)_2•6 H_2O, \geq 98\%$, Sigma–Aldrich, USA) and manganese nitrate $(Mn(NO_3)_2•4 H_2O, \geq 97\%$, Sigma–Aldrich, USA) were dissolved in distilled and deionized (DDI) water (Vivagen Co., Ltd., South Korea) to prepare a 2 mol L^{-1} concentration (Table S3). Sodium carbonate $(Na_2CO_3, \geq 99.5\%$, Sigma-Aldrich) was dissolved in DDI at a concentration of 2 mol L^{-1}, which was used as a precipitant. Then 40 mL of the $Co(NO_3)_2•6 H_2O$ and $Mn(NO_3)_2•4 H_2O$ solution and 40 mL of the Na_2CO_3 solutions were then added dropwise to 50 mL DDI water with vigorous stirring at 25 °C while maintaining the pH of the solution mixture at 8.0 ± 0.1. The dropwise addition led to the formation of a light purple precipitate. After stirring for 6 h in an airtight bottle, the solution was aged for 6 h without stirring at 25 °C. The aged suspension was then centrifuged four times with DDI water at 4000 rpm, filtered, and washed with DDI water; the collected powder was dried at 100 °C for 12 h. Finally, the dried powder was calcined at 330 °C under an airflow condition (flow rate of 100 mL h^{-1}) for 3 h.

2.2. CO_2 hydrogenation

The CO_2 conversion was evaluated in a continuous fixed-bed reactor. A detailed description of the reactor system has been presented in our previous paper [14]. A brief description is provided here. A stainless-steel tubular reactor with a 10 mm inner diameter was used. For each reaction, 1 g of the catalyst was mixed with 3 g of silica as a thermal diluent (Fischer Chemicals, S/0365/60), and the mixture was fixed in the middle of the reactor using quartz wool. The catalyst was pre-reduced under a H_2 at a flow rate of 50 mL min^{-1} for 6 h at 350 °C, 4.0 MPa, ramping rate of 2.5 °C min^{-1}. After the catalyst pre-reduction, the temperature of the reactor was reduced to the experimentally

desired temperatures of 230–310 °C, and the gas flow was switched from H_2 to the CO_2/H_2 mixture. During CO_2 hydrogenation, the product stream was passed through a condenser whose temperature was maintained at 75 °C to collect the liquid product; the noncondensed gaseous product stream was directed towards a refinery gas analyzer gas chromatograph (RGA–GC, PerkinElmer Clarus 580 GC-Model Arnel 1115PPC, PerkinElmer, USA) that was connected on line to the reactor system. A detailed description of the RGA–GC specifications is presented elsewhere [15]. Using the RGA–GC, C_1–C_5 hydrocarbons were quantified. The liquid products were collected by adding dichloromethane (DCM, >99.9%, Sigma–Aldrich, USA) and proceeding liquid–liquid separation. Liquid hydrocarbon and some oxygenated species dissolved in the DCM phase and the other oxygenate species dissolved in the water phase were analyzed using gas chromatography-time of flight mass spectrometry (GC–TOF/MS) and high-performance liquid chromatography (HPLC), respectively. The GC and TOF/MS instruments were manufactured by Agilent Technologies (model 7890A; USA) and the LECO Corporation (model Pegasus HT; USA), respectively. The GC–TOF/MS system was equipped with a Rxi-5sil MS column (30 m × 0.25 mm × 0.25 μm, RESTEK, USA). The GC-TOF/MS and analysis conditions are described in detail in our previous paper [16]. The liquid products were quantified using GC equipment with an Rxi-5 sil-MS column (30 m × 0.25 mm × 0.25 μm, RESTEK, USA) and a flame ionization detector (FID). The effective carbon number (ECN) method was used for the quantification of liquid products in the range from C_5 (which was remained in the liquid phase) to C_{19} by constructing calibration curves using a standard compound (n-decane). The ECN method is explained in detail in our previous paper [14]. Heavy wax was analyzed using the PerkinElmer model Clarus 600 GC equipped with an on-column injector, FID, and SimDis capillary column (polymethylsiloxane; dimensions = 10 m × 0.53 mm × 1.0 μm). The SimDis result was calibrated with a known concentration of n-decane (which was measured by GC–FID) in the liquid product. Under an assumption that the n-decane content measured by GC–FID should be the same with the n-decane content measured by SimDis, other long chain hydrocarbons (C_{20}–C_{60}). The water phase was analyzed by HPLC (Alliance, model e2695; waters, USA) equipped with an Aminex HPX-87 H ion exclusion column (300 mm × 7.8 mm) and an ultraviolet-visible (UV–vis) detector.

Hydrocarbons were quantified based on the carbon mole% (C-mol%) for all tested catalysts. The carbon balance obtained in the catalytic performance test after quantifying the gas and liquid products was > 95%. The CO_2 conversion, CO selectivity, hydrocarbon selectivity, and hydrocarbon yield were calculated using Eqs. (1)–(4).

$$CO_2 \text{ conversion (C − mol\%)} = \frac{CO_{2\,in} - CO_{2\,out}}{CO_{2\,in}} \times 100\% \qquad (1)$$

$$CO \text{ selectivity (C − mol\%)} = \frac{CO_{out}}{CO_{2\,in} - CO_{2\,out}} \times 100\% \qquad (2)$$

$$Hydrocarbon \text{ selectivity (C − mol\%)} = \frac{\text{Moles } of\ C_i \text{ hydrocarbon } \times i}{CO_{2\,in} - CO_{2\,out}} \times 100\% \qquad (3)$$

$$Hydrocarbon \text{ yield (C − mol\%)} = \frac{\sum_{i=1} C_i H_j \,(\text{including CO}) \times CO_2 \text{ Conversion}}{100} \qquad (4)$$

$$\text{Carbon } balance \text{ (C} - \text{mol\%)} = \frac{CO_{out} + \sum_{i=1}^{n=5} RGA - GC, C_iH_j + \sum_{i=1}^{n=5} HPLC, C_iH_jO_k + \sum_{i=6}^{n=19} GC - FID, C_iH_j + \sum_{i=20} SimDist}{CO_{2\,in} - CO_{2\,out}} \tag{5}$$

2.3. Catalyst characterization

The crystalline structures of the catalysts were characterized using a Rigaku X-ray diffractometer (XRD; D/Max–2500 V/PC, Japan) with Ni-filtered Cu-Kα radiation (λ = 1.5418 Å, 40 kV, and 50 mA). The XRD patterns were collected at a 2θ range of 5–90° at a scanning step of 0.02° and a scan rate of 2° min^{-1}. The morphologies of the catalysts were observed using field emission scanning electron microscopy (FE–SEM; S-4100, Hitachi, Japan). A microstructure analysis was conducted using Cs-corrected scanning transmission electron microscopy (STEM; TitanTM 80–300, FEI, USA) equipped with a fast CCD camera (Gatan, Oneview 1095) and an electron energy loss spectrometer (Gatan, Quantum 966). The microstructure and elemental mapping analyses of the prepared samples were investigated using a high-resolution transmission electron microscope (HR–TEM; FEI Talos F200X, USA) equipped with an energy-dispersive X-ray spectrometer (EDX; Super-X EDX, Bruker, USA) operating at 200 keV. Textural properties of the catalysts were determined by acquiring their nitrogen adsorption–desorption profiles at − 196 °C using a Belsorp-mini II instrument (BEL Inc., Japan). The specific surface areas of the catalysts were determined using the multipoint Brunauer–Emmett–Teller (BET) method. Pore-size distributions were calculated from Barrett–Joyner–Halenda (BJH) plots to analyze the mesoporosities of the catalyst. Before sample measurement, the catalysts were pre-treated under vacuum at 120 °C for 6 h to remove absorbed moisture and other light species. The amounts of metallic species (Fe, Al, and Na) in the catalysts were determined using inductively coupled plasma–optical emission spectrometry (ICP–OES; Optima 7300 V, PerkinElmer, USA).

The temperature-programmed desorption of hydrogen (H$_2$–TPD) was performed using a BELCAT-M instrument (BET Inc., Japan) equipped with a thermal conductivity detector (TCD). An aliquot (0.07 g) of catalyst was added to the quartz sample tube. Before H$_2$ adsorption, the sample tube was reduced at 350 °C under a ramping rate of 2.5 °C min^{-1} and under ultrahigh purity 5% H$_2$/Ar gas (99.999%, JC Gas Company, South Korea) injected at a flow rate of 40 mL min^{-1} for 6 h. Then, the sample tube was naturally cooled to 50 °C and the catalyst was completely saturated with 5% H$_2$/Ar at a flow rate of 40 mL min^{-1} for 1 h. Ultrahigh purity Ar gas (99.999%, JC Gas Company, South Korea) was used to flush the entire system at a flow rate of 40 mL min^{-1} for 30 min at 50 °C to remove physically adsorbed H$_2$ molecules. Next, the temperature of the sample tube was increased to 900 °C at a heating rate of 5 °C min^{-1} and under a ultrahigh purity Ar gas flow rate of 40 mL min^{-1} for the H$_2$–TPD analysis.

The temperature programmed desorption of carbon dioxide (CO$_2$–TPD) was conducted to examine the basicity of the catalyst. Each catalyst (0.07 g) was reduced at 350 °C at a ramping rate of 2.5 °C min^{-1} under an ultrahigh purity 5% H$_2$/Ar gas injected at a flow rate of 40 mL min^{-1} for 6 h. After the sample was naturally cooled to 50 °C, a continuous flow of pure CO$_2$ (99.995%, JC Gas Company) was injected into the sample tube at a flow rate of 40 mL min^{-1} for 1 h to saturate the catalyst completely. The system was then flushed with ultrahigh purity He (99.995%, JC Gas Company) for 30 min at a flow rate of 40 mL min^{-1} to remove any physiosorbed CO$_2$ molecules. The CO$_2$ desorption experiment was conducted by heating the catalyst samples up to 900 °C at a heating rate of 5 °C min^{-1} under He at a flow rate of 50 mL min^{-1}.

The temperature-programmed desorption of carbon monoxide (CO–TPD) was conducted to examine the CO adsorption. Each catalyst (0.07 g) was reduced at 350 °C at a ramping rate of 2.5 °C min^{-1} under a ultrahigh purity 5% H$_2$/Ar gas injected at a flow rate of 40 mL min^{-1} for 6 h. After the sample was naturally cooled to 50 °C, a continuous flow of mixed CO/He (5% CO/He, JC Gas Company) was injected into the sample tube at a flow rate of 40 mL min^{-1} for 1 h to completely saturate the catalyst. Then, the system was flushed with ultrahigh purity He (99.995%, JC Gas Company) for 30 min at a flow rate of 40 mL min^{-1} to remove any physiosorbed CO molecules. The CO desorption experiment involved heating the catalyst samples up to 900 °C at a heating rate of 5 °C min^{-1} under He at a flow rate of 40 mL min^{-1}.

The reduction properties of the catalysts were analyzed by collecting H$_2$ temperature-programmed reduction (H$_2$–TPR) profiles using the BELCAT-M instrument. A known amount of catalyst (0.07 g) was added to the quartz sample tube. Prior to H$_2$ adsorption, the sample tube was heated to 250 °C at a ramping rate of 10 °C min^{-1} under an ultrahigh-purity Ar gas (99.999%, JC Gas Company) flow rate of 40 mL min^{-1}; the temperature was maintained at 250 °C for 2 h to remove any adsorbed water or volatile species. The sample tube was then naturally cooled to 50 °C, and the catalyst was completely saturated with 5% H$_2$/Ar at a flow rate of 50 mL min^{-1} for 1 h. Then, the temperature of the sample tube was increased to 700 °C at a heating rate of 5 °C min^{-1} under a flow of 5% H$_2$/Ar at 40 mL min^{-1} for the H$_2$–TPR analysis. Effluent species during the H$_2$–TPR analysis were measured using a temperature-programmed hydrogenation mass spectrometer (TPH–MS, QMS 200 M2, Pfeiffer, USA).

X-ray photoelectron spectroscopy (XPS) was conducted using an ESCALAB250Xi (Thermo scientific, UK) spectrometer. The peak assignments were referenced to the C–C bond at 284.8 eV. Co K-edge and Mn K-edge X-ray absorption spectroscopy (XAS) were performed in the transmission mode at the 10 C beamline of the Pohang Accelerator Laboratory using a Si(111) double crystal monochromator. For energy calibration, the reference spectra of Co, CoO, and Co$_3$O$_4$ powders were obtained simultaneously. X-ray absorption near edge structure (XANES) and extended X-ray absorption fine structure (EXAFS) data were processed using Athena/Artemis software packages. Further, Fourier transformed k^3-weighting was performed in the k-range of 3.0–11.0 Å with a fitting R-space within the ∆R region of 1.0–3.0 Å.

For CO$_2$ and CO, diffuse reflectance infrared Fourier transform spectroscopy (DRIFTS) analyses were conducted to investigate reaction intermediate species formed during the CO$_2$ hydrogenation reaction over the CMO-0 and CMO-10 catalysts. A PerkinElmer Frontier spectrometer equipped with a Harrick Praying Mantis cell (USA) and a mercury cadmium telluride (MCT) detector was used for the DRIFTS analyses. All fresh catalyst samples (mixed with KBr at a weight ratio of 5:95) were pre-reduced in the cell at 350 °C and 3.0 MPa under pure H$_2$ flow at a rate of 50 mL min^{-1} for 6 h. After the pre-reduction, the cell was cooled to ambient temperature and background spectra were collected. In the first set of measurements, the CO$_2$ DRIFTS analysis was conducted by flowing CO$_2$ (99.995%) at 50 mL min^{-1} and under 0.1–3.0 MPa. The pressure of the cell was controlled using a back-pressure regulator (26–2300 Series, Tescom, USA). IR spectra were collected at different temperatures in the range 50–270 °C with a ramping rate of 2.5 °C min^{-1}. Once steady state conditions were established at 270 °C (after approximately 30 min), the CO$_2$ gas was switched to H$_2$ gas at 270 °C, 3.0 MPa, and 50 mL min^{-1}; then, the IR spectra were collected for CO$_2$ hydrogenation for 6 h. A similar procedure was adopted to perform CO DRIFTS analysis with 5% CO/He to

investigate CO adsorption, and subsequently, the CO hydrogenation over the catalysts. In the second set of the measurements, CO_2 and H_2 (H_2/CO_2 ratio of 3:1) were co-injected into the DRIFTS cell cooled down to 270 °C after the pre-reduction of the catalysts at 350 °C and 3.0 MPa. At 270 °C, the IR spectra for the CO_2 hydrogenation were collected until 120 min, and then, the flow gas was switched to H_2 (at 50 mL min^{-1}) and the H_2 flow was maintained for 360 min to investigate reaction kinetics. Similar DRIFTS analyses were performed at varying pressures of 0.1–3.0 MPa and temperatures of 200–300 °C over the CMO-0 catalyst for understanding the effect of pressure and temperature on CO_2 hydrogenation that compares the intensities of the peak associated with reaction intermediates and products formed during the DRIFT analyses.

2.4. Computational details

Density functional theory (DFT) implemented in the Vienna Ab-Initio simulation package [17] was used for the mechanistic investigations of CO_2 hydrogenation on Co, Co carbide, and Co oxide surfaces. The electronic structure was described using the vdW-DF2 exchange correlation functional within a generalized gradient approximation [18]. The convergence criteria of the electronic and ionic optimization were set to 10^{-4} and 10^{-3} eV, respectively. The bulk structures of Co (space group, $P63/mmc$), Co_2C (space group, $Pmnn$), and Co_3O_4 (space group, $Fd3m$) were optimized using $16 \times 16 \times 16$ k-points sampling. The surface structure of Co (0001), Co_2C (101), and Co_3O_4 (110) were generated for catalysis modelling based on previous studies that reported the stability of the surface structure [19,20]. Although the Co_3O_4 (111) and CoO (001) (space group, $Fm3m$) surfaces [21,22] were tested in this study, their surface structures were unstable and collapsed when the adsorbates attached. The oxygen vacant site of Co_3O_4 (vac-Co_3O_4) was constructed by removing an oxygen atom from the Co_3O_4 (110) surface

(Fig. 6B). The surface slabs of all three materials contained $4 \times 4 \times 4$ Co atoms in the x, y, and z directions, where the bottom two layers were constrained to the bulk-optimized geometry while the upper two layers were fully allowed to relax. The interaction between the slabs was prevented by adding 10 Å of vacuum in the z direction. Surface slab calculations and the system catalysis were conducted using $4 \times 4 \times 1$ k-points sampling with a Monkhorst–Pack mesh grid.

The free energy of a reaction ΔG was calculated using

$$\Delta G = \Delta E + \Delta E_{ZPE} + \Delta \int_0^T C_P dT - T\Delta S$$

where E, E_{ZPE}, C_P, T, and S denote the electronic energy obtained from the DFT calculation, zero-point energy, heat capacity, temperature, and entropy of a species, respectively. The ideal gas and harmonic approximations were adopted for the gas and surface molecules, respectively. E_{ZPE}, C_P, and S were calculated using vibrational frequencies obtained through the normal mode analysis [23]. The transition state of a reaction was obtained using the Bayesian transition state search module implemented in CatLearn [24].

3. Results and discussion

3.1. CO_2 hydrogenation performance

The catalytic performances of CMO-y catalysts with varying Mn contents were evaluated, and the results are illustrated in Fig. 1. The CMO-10 catalyst with a Na content of 0.12 wt% exhibited a high CO_2 conversion of 64.3% with a significantly high C_{5+} selectivity of 32.9%, whereas its selectivity toward CO was highly suppressed (0.2%). When CO was included in the hydrocarbon selectivity calculation, the C_{5+} yield was 21.1%, which is unprecedently higher than that of previously
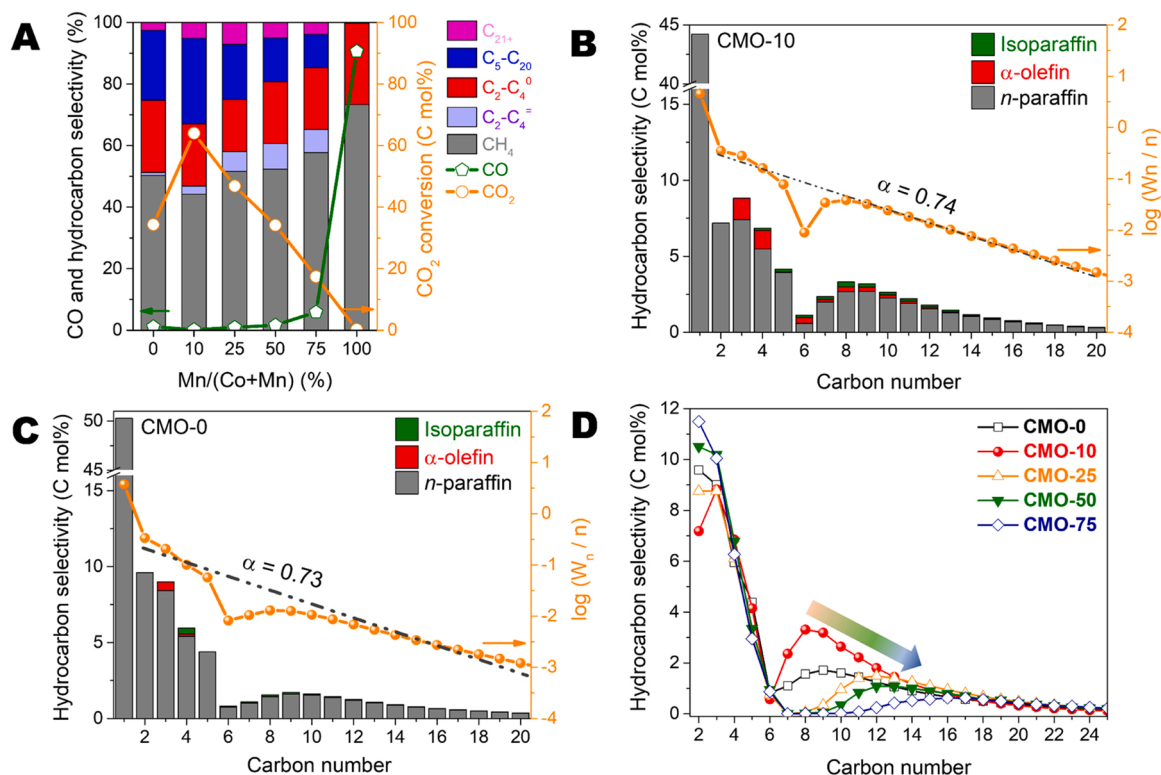

Fig. 1. (A) CO_2 conversion and product selectivity over CMO-y catalysts with varying Mn contents. Distribution of hydrocarbons with respect to their carbon number (n) produced over (B) the CMO-10 catalyst and (C) the CMO-0 catalyst. (D) Comparison of hydrocarbon selectivity with respect to n over CMO-y catalysts. W_n represents the weight fraction of hydrocarbons with respect to their n. Reduction conditions: Ramping rate = 2.5 °C min^{-1}, temperature = 350 °C, pressure = 4.0 MPa, and H_2 flow rate = 50 mL min^{-1} for 6 h. Reaction conditions: Temperature = 270 °C, pressure = 4.0 MPa, H_2/CO_2 = 3:1, and GHSV = 4000 mL g^{-1} h^{-1} (CO_2 = 1000 mL g^{-1} h^{-1}; H_2 = 3000 mL g^{-1} h^{-1}) for 125 h.

reported Co-based catalysts (0–1.4%) and even comparable than that of previously reported Fe-based catalysts (11.7–26.4%) at GHSV $\geq$ 4000 mL g^{-1} h^{-1} (Table S1 and Fig. S1A). Thus, the CO_2 conversion behavior of the CMO-10 catalyst is unlike that of previously reported Co-based catalysts, which produced considerable volumes of methane (70–100%) with small fractions of C_2–C_4 and negligible fractions of C_{5+} (Table S1). The chain growth probability of C_{2+} products over the CMO-10 catalyst was 0.74, which is close to that of the Co-based FTS reaction (0.65–0.95) [25]; however, it is considerably higher than that of other Co-based catalysts used in CO_2 conversion (<0.25) [9]. In addition to the high C_{5+} selectivity, the CMO-10 catalyst also exhibited high selectivities toward CH_4 (44.2%) and C_2–C_4 (22.9%). Therefore, both high-yield gaseous and liquid fuels were produced over the catalyst via a single-pass CO_2 stream. The C_{5+} yield of the CMO-10 catalyst is comparable to that of Na–Fe_3O_4/HZSM-5 [26], Fe_2O_3 @KO_2/ZSM-5 [27], FeAlO$_x$-5/HZSM-5 [14], and $ZnFeO_x$/HZSM-5 [28], but it is considerably higher than that of the other metal oxides/HZSM-5 composite catalysts (0.2–14.1%) when GHSV $\geq$ 4000 mL g^{-1} h^{-1} (Table S2 and Fig. S1B). Further, C_{5+} hydrocarbons produced over the CMO-10 catalyst comprise linear paraffins with small fractions of branched hydrocarbons (2.5%) and olefins (4.5%), as indicated in Fig. 1B; the overall olefin/paraffin ratio in the product is very low (0.07%). The formation of oxygenated species is negligible (<0.6%, Fig. S2). Attempting to increase C_{5+} yield using metal oxide/zeolite composite catalysts eventually leads to the production of a large fraction of aromatics. The aromatic contents in the produced C_{5+} fraction over metal oxide/HZSM-5

composite catalysts were in the range of 60–90% (Table S2). When considering strict regulations for aromatic contents in transportation fuels, a high selectivity toward aromatics needs to be carefully addressed [29]. Further, one-pass CO_2 conversion over the Fe-based catalysts is < 40% with high residual CO selectivities of up to 15% at GHSV $\geq$ 4000 mL g^{-1} h^{-1} (Tables S1 and S2). This would necessitate an effluent recycling unit or a two-stage RWGS and FTS reaction system with a water removal unit [30,31] when implemented on a practical scale. Therefore, the CMO-10 catalyst has clear advantages over Fe-based catalysts given its high CO_2 conversion, high-yield hydrocarbons, negligible selectivity toward CO, and low reaction temperature.

The CMO-y catalyst with varying Mn contents exhibited stable CO_2 conversion performance during 125 h on the stream (Fig. S3). As expected, negligibly small CO_2 conversion (<0.3%) was observed over MnO_2 without Co, indicating the manganese oxide is not an active site for CO_2 conversion (Fig. 1A). Even without the Mn promoter, the CMO-0 catalyst exhibited a high CO_2 conversion of 34.3% and high selectivity toward C_{5+} (25.3%) with highly suppressed selectivity toward CO (1.1%). The C_{5+} yield over the CMO-0 catalyst (including CO) was 8.7%, which is higher than that over most previous pure Co-based catalysts (Table S1). The chain growth probability over the CMO-0 catalyst was slightly lower than that over the CMO-10 catalyst (Fig. 1B and C). Further, the chain growth probability increased as the Mn content increased in the CMO-y catalyst, resulting in the formation of longer-chain hydrocarbons (Fig. 1D); for example, over the CMO-75 catalyst, C_{10+} is a major liquid hydrocarbon species. Thus, the presence of the Mn
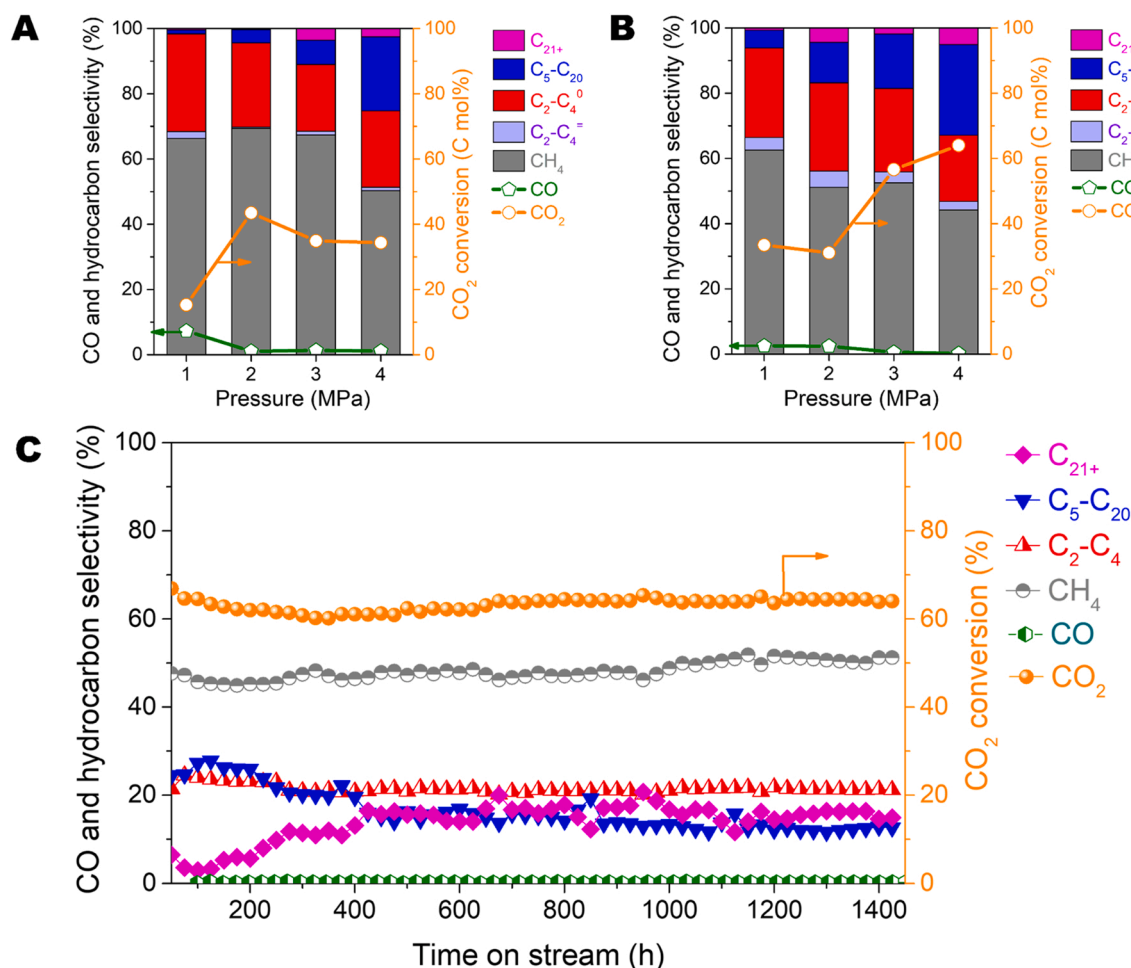

Fig. 2. CO_2 conversion and product selectivity at varying pressures over (A) the CMO-0 catalyst and (B) the CMO-10 catalyst. (C) Long-term stability of the CMO-10 catalyst. Reduction conditions: Ramping rate = 2.5 °C min^{-1}, temperature = 350 °C, pressure = 4.0 MPa, H_2 flow rate = 50 mL min^{-1} for 6 h. Reaction conditions: Temperature = 270 °C, pressure = 4.0 MPa, H_2/CO_2 = 3:1, and GHSV = 4000 mL g^{-1} h^{-1} (CO_2 = 1000 mL g^{-1} h^{-1}; H_2 = 3000 mL g^{-1} h^{-1}).

promoter suppressed the chain termination reaction.

The role of reaction pressure in CO_2 conversion and C_{5+} selectivity was examined by varying the pressure (1.0–4.0 MPa) over the CMO-0 and CMO-10 catalysts (Fig. S4). Results collected after 125 h on the stream are shown in Fig. 2A and B. A high reaction pressure was beneficial in increasing C_{5+} selectivity over the CMO-0 catalyst. In typical syngas conversion, a shift in the product distribution to the C_{5+} fractions with an increase in pressure is attributed to a decrease in the H/C coverage [32] and the enhanced readsorption of C_2–C_4 olefins [32]. The

reaction pressure had a more profound effect on CO_2 conversion over the CMO-10 catalyst than that on the CMO-0 catalyst (Fig. 2B). Thus, the high reaction pressure and Mn promotor facilitated the chain propagation reactions.

The CO_2 hydrogenation performance of the CMO-10 catalyst was also investigated by varying reaction parameters to determine the optimum condition (Fig. S5). The methanation activity over the CMO-10 catalyst increased under the conditions of high temperature (310 °C), high H_2/CO_2 ratio (4:1), and high GHSV (12000 mL g^{-1} h^{-1}). A similar
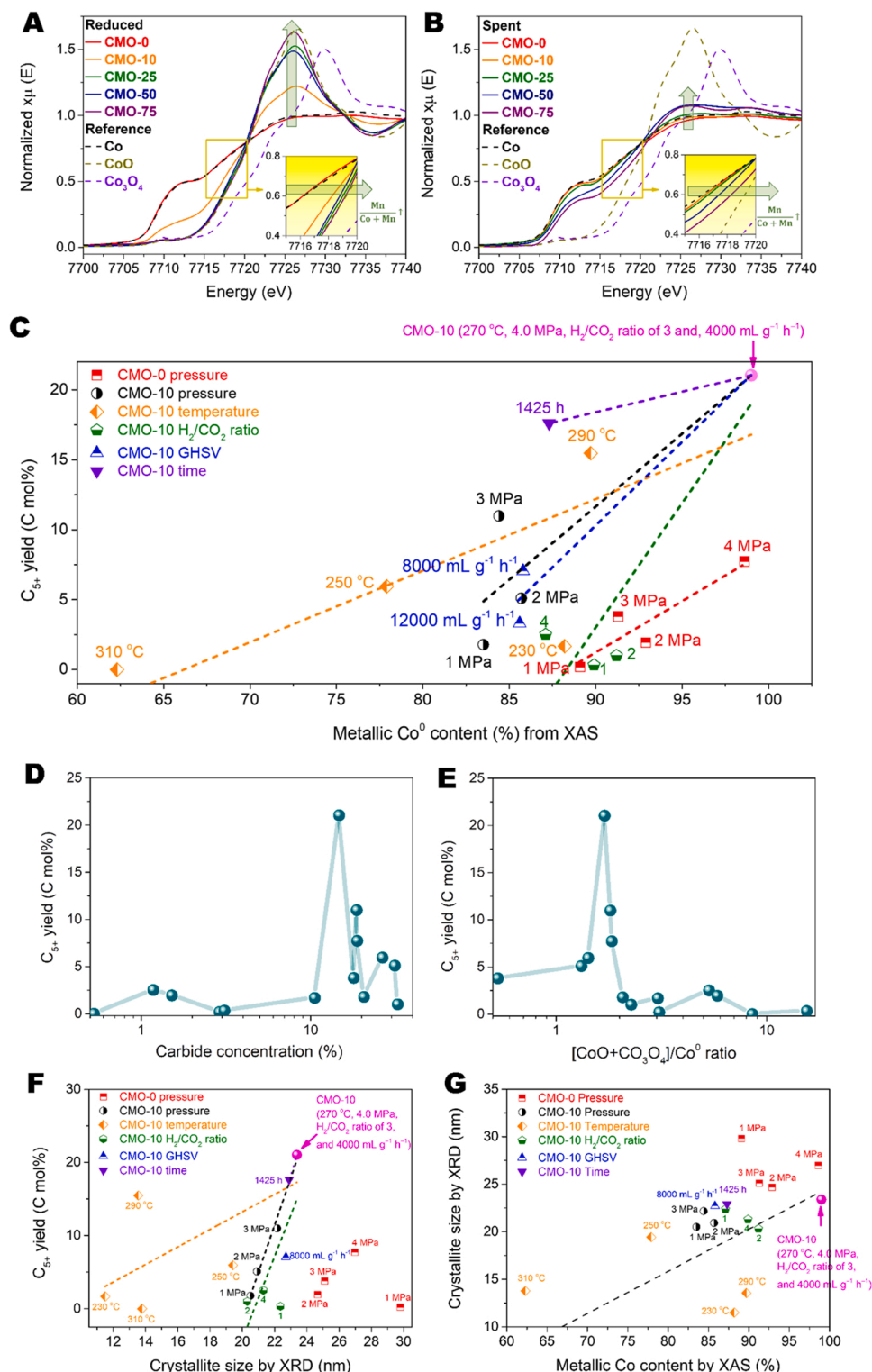

Fig. 3. Normalized Co K-edge XANES spectra. (A) Reduced CMO-*y* catalysts and (B) spent CMO-*y* catalysts. Correlations (C) between metallic Co content estimated by the linear combination fitting of the XANES spectra and the C_{5+} yields, (D) between surface carbide concentration estimated by the C 1 s XPS spectra and the C_{5+} yield, (E) between [CoO+Co_3O_4]/Co^0 ratio estimated by the C 1 s XPS spectra and the C_{5+} yield, (F) crystallite size of Co measured by XRD and the C_{5+} yield, and (G) metallic Co content estimated by the linear combination fitting of the XANES spectra and the crystallite size of Co measured by XRD.

behavior has been observed in typical FTS reactions of syngas [33]. Further, enhanced methanation at a high temperature of 310 °C and a high H_2/CO_2 ratio of 4:1 is similar to CO_2 conversion over Co-based catalysts [5,9]. Therefore, the unexpectedly high C_{5+} selectivity over the CMO-10 catalyst at 270–290 °C, H_2/CO_2 ratio of 3:1, and GHSV of 4000 mL g^{-1} h^{-1} indicates that the CMO-10 catalyst can establish a dominant FTS regime over the methanation regime under these reaction conditions.

Fig. 2C shows the long-term stability of the CMO-10 catalyst. The CMO-10 catalyst exhibited good stability to long-chain hydrocarbons in the hydrogenation of CO_2. Stable CO_2 conversion and C_{5+} selectivity up to 1425 h on the stream indicate that the sintering of active sites and the deposition of polymeric carbon or coke play minor roles in ensuring the long-term stability of the CMO-10 catalyst. Product distribution in C_{5+} changed with increasing time on the stream; C_5–C_{20} selectivity decreased from 24.5% to 12.6%, whereas C_{21+} selectivity increased from 6.5% to 14.9% with an increasing time on the stream from 25 to 1425 h. The partial poisoning of the FTS sites by continuous accumulation of highly resistant graphitic carbon with increasing time on stream could contribute to increase the chain growth probability [33, 34]. The presence of C_{20}–C_{50} in the product was observed in the simulated distillation profile of the liquid product (Fig. S6). Therefore, gaseous/liquid fuel and lube base oil fractions were produced over the CMO-10 catalyst.

3.2. Characterization of CMO-y catalysts

The crystalline structures of fresh, reduced, and spent CMO-0 and CMO-10 catalysts were examined using XRD (Fig. S7). The Mn promotor inhibited the complete reduction of Co_3O_4 to metallic Co during H_2 reduction, which resulted in mixed CoO and hcp Co phases with small fractions of the fcc Co phase. In the spent CMO-10 catalyst, the CoO phase was reduced to hcp Co with small fractions of fcc Co and $MnCO_3$. As the Mn content in the reduced CMO-y catalysts increased from 25% to 75%, peaks associated with CoO at 36.6° and 42.6° progressively downshifted to MnO at 35.0° and 40.7°, respectively (Fig. S8); this indicates the formation of spinel-structured $Co_xMn_{3-x}O_4$ ($0 < x < 3$) [35]. The spinel $Co_xMn_{3-x}O_4$ and bulk Co_2C phases were not observed in the spent CMO-y catalysts (Fig. S9). At 270–290 °C, metallic Co and $MnCO_3$ phases were found to be the major species in the spent CMO-10 catalyst. At 310 °C, the intensity of the peaks associated with metallic Co and $MnCO_3$ phases decreased significantly (Fig. S10). These results suggest that structural collapse occurred at a high reaction temperature. The Mn promoter reduced the crystallite size of Co_3O_4 during calcination (Table S4); further, the crystallite size of Co_3O_4 in the fresh CMO-10 catalyst (5.9 nm) was considerably smaller than that of the CMO-0 catalyst (9.7 nm). After reduction, the CMO-0 and CMO-10 catalysts exhibited similar crystallite sizes of hcp and fcc Co (20–23 nm). In the spent CMO-0 catalyst, the crystallite sizes of hcp Co and fcc Co increased significantly to 27.0 and 34.5 nm, respectively. In contrast, in the spent CMO-10 catalyst, the crystallite size of hcp Co and fcc Co increased only slightly to 23.4 and 21.4 nm, respectively. Therefore, the Mn promoter suppressed the crystal growth of metallic Co during CO_2 hydrogenation.

Oxidation states and local chemical structures of the reduced and spent CMO-y catalysts were analyzed using XAS. The Co K-edge XANES spectrum of the reduced CMO-0 catalyst was similar to that of the metallic Co standard, which exhibits an almost complete reduction of Co_3O_4 to the metallic Co phase (Fig. 3A). The local and long-range order characteristics of the reduced CMO-y catalysts with Mn contents $\geq$ 25% approached that of the CoO standard. For the reduced CMO-10 catalyst, both the metallic Co^0 and CoO_x characteristics coexisted. In the k^3-weighted Fourier-transform magnitudes of the Co K-edge extended EXAFS spectrum of the reduced CMO-0 catalyst (Fig. S11A), the peak at 2.50 Å is assigned to the Co–Co bond of hcp Co [36]. Two additional peaks at 2.14 and 3.03 Å were observed for the reduced CMO-10 catalyst, and these peaks correspond to the Co–O and Co–Co bonds of CoO

[36], respectively. The metallic Co content in the reduced CMO-y catalyst was calculated using the linear combination fitting of the XANES spectra (Table S5). The Mn-promoter in the CMO-y catalyst suppressed the reducibility of Co. The low reducibility of the Mn-rich CMO-y catalysts can be attributed to the enhanced formation of spinel-structured $Co_xMn_{3-x}O_4$ with increasing Mn content.

The transformation of CoO to metallic Co was observed in the XANES spectra of the spent CMO-y catalysts (Fig. 3B). Metallic Co is the dominant species in the spent CMO-y catalysts with $y \leq 25\%$ (93–99%; Table S5). The Co K-edge EXAFS spectra of the spent catalysts present one prominent peak centered at 2.50 Å, which is associated with the Co–Co bond of hcp Co (Fig. S11B). As the Mn content increased from 25% to 75%, the onset of the adsorption edges in the XANES spectra upshifted, and the height of the white line peak increase, indicating the CoO and Co_3O_4 phases increased in the spent catalysts.

The active site for the synthesis of long-chain hydrocarbons from syngas has been shown to be the metallic Co phase [7]. Changes in the local chemical structures of the spent CMO-y catalysts at varying reaction conditions were investigated using XAS to examine the correlation between the metallic Co phase and C_{5+} yields (Figs. S12 and S13). Under the conditions that resulted in high-yield C_{5+}, the metallic Co contents in the spent CMO-y catalysts were found to increase. The positive correlation between the metallic Co content in the CMO-y catalysts and the C_{5+} yields is shown in Fig. 3C. Under the conditions of the FTS-dominant regime, the metallic Co content was $> 98\%$; in the methanation-dominant regime, the metallic Co content was 60–90%. Therefore, high metallic Co content is a prerequisite for establishing the FTS regime in CO_2 hydrogenation similar to the case of syngas conversion. In the CoO phase in the CMO-10 catalyst collected at 310 °C, the coordination number of the Co–O bond in CoO was 2–3 times higher than that of Co–Co (Table S7), implying that CoO formed in the methanation regime exhibited an oxygen-rich nanocluster structure. For the chemical structure of the Mn promoter, various oxidation states of Mn such as MnO_2, Mn_2O_3, Mn_3O_4, and MnO coexisted in the reduced CMO-y catalysts (Fig. S14 and Table S6). In the spent CMO-y catalyst, the dominant Mn species was $MnCO_3$ with small fractions of Mn_2O_3, Mn_3O_4, and MnO. The $MnCO_3$ content increased from 93.7% to 98.3% with an increase in the reaction time from 125 to 1425 h.

The surface chemical environments of the fresh, reduced, and spent CMO-10 catalysts were examined using XPS (Fig. S15). The spent CMO-10 catalyst collected after 125 h on the stream reaction exhibited a new peak at 283.2 eV, which could be assigned to Co_2C [37]. Thus, at the initial stage of the reaction, surface atomic carbon species dissociated from the adsorbed CO_2 species reconstructed the Co surface, which led to the formation of Co_2C. As the reaction time increased from 125 to 1425 h, the area% of Co_2C in the spent catalyst increased from 14.7% to 29.1%. A metallic Co peak at 778.4 eV [36] appeared in the Co 2p spectrum of the reduced CMO-10 catalyst; the area% of the metallic Co was small (8.7%) because of the incomplete reduction of the Mn-promoted catalyst. This agreed well with the XRD and XAS results. In the spent CMO-10 catalysts collected after 125 and 1425 h on the stream reaction, the area% of metallic Co and Co_2C peaks at 778.4 eV increased to 28.7% and 27.6%, respectively. In the O 1 s spectra, the two major peaks at 529.6 and 531.2 eV could be assigned to the lattice oxygen of the metal oxide and oxygen vacancies [38]. The area% of the peak associated with oxygen vacancies in the spent catalyst increased from 26.8% (reduced catalyst) to 53.4% (after 1425 h on the stream reaction). In the spent CMO-10 catalyst collected after 125 h on the stream reaction, the major Mn species was Mn^{2+}. The chemical environment changes at the surface of the CMO-0 catalyst during the reduction and CO_2 hydrogenation were similar to those of the CMO-10 catalyst (Fig. S16). Even without the Mn promoter, the complete reduction of Co oxides to metallic Co did not occur at the surface of the reduced CMO-0 catalyst; the reduction temperature of 350 °C was not sufficiently high for this complete transformation.

The XPS profiles of the spent CMO-0 and CMO-10 catalysts at varying

reaction conditions were collected (Figs. S17–20) to examine any possible correlation between the surface chemical species of the catalyst and the C_{5+} yield; the results are shown in Fig. 3D and E. The C_{5+} yield was maximized at the carbide area% of 14.7% and the $[CoO + Co_3O_4]/Co^0$ ratio of 1.7. Therefore, some fractions of Co_2C and CoO_x need to be present on the catalyst surface to establish FTS regime in CO_2 hydrogenation.

The morphology of the fresh, reduced, and spent CMO-0 and CMO-10 catalysts were examined using HR–TEM, SEM, and STEM–EDX. The fresh CMO-0 catalyst exhibited spherical-shape Co_3O_4 nanoparticles (NPs) with an average diameter of 9.0 nm (Fig. S21). The high-angle annular dark-field STEM (HAADF–STEM) and EDX images showed a uniform distribution of Na over the entire catalyst. In the fresh CMO-10 catalyst, the average diameter of the Co_3O_4 NPs was further reduced to 5.1 nm (Fig. S22). The particle sizes of the fresh CMO-10 catalysts estimated using HR–TEM were similar to their crystallite sizes (Table S4); this indicates a single crystalline structure. Thus, the Mn promotor suppressed the crystalline growth of Co_3O_4 during calcination.
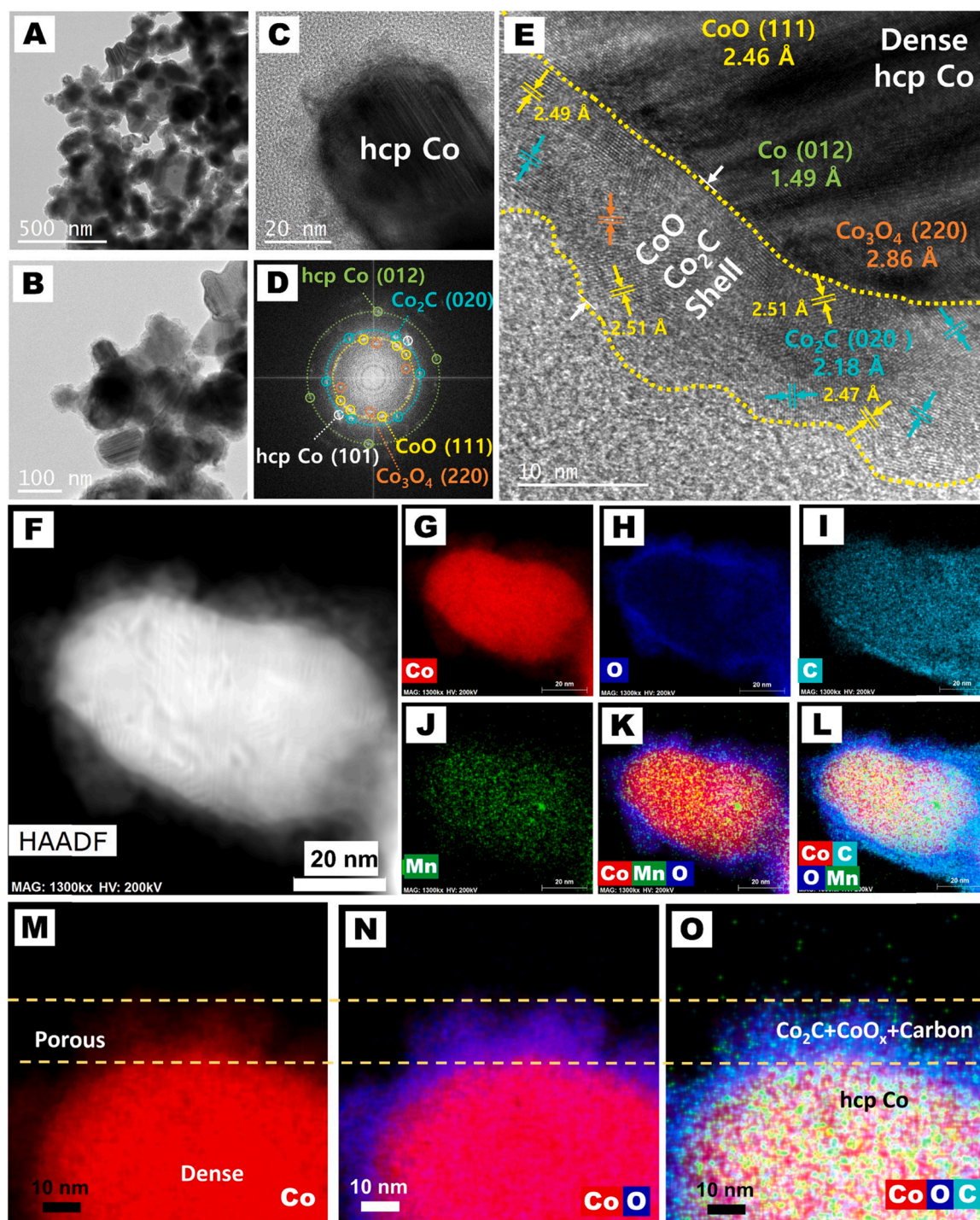

Fig. 4. (A–C, and E) HR–TEM and (D) FFT images of the spent CMO-10 catalyst. (F) HAADF–STEM image and its corresponding EDX images of (G) Co; (H) O; (I) C; (J) Mn; (K) Co, Mn, and O; (L) Co, Mn, C, and O. Magnified outermost shell layer of (M) Co; (N) Co and O; and (O) Co, O, and C. Reduction conditions: Ramping rate = 2.5 °C min^{-1}, temperature = 350 °C, pressure = 4.0 MPa, H_2 flow rate = 50 mL min^{-1} for 6 h. Reaction conditions: Temperature = 270 °C, pressure = 4.0 MPa, H_2/CO_2 = 3:1, GHSV = 4000 mL g^{-1} h^{-1} (CO_2 = 1000 mL g^{-1} h^{-1}; H_2 = 3000 mL g^{-1} h^{-1}) for 125 h.

Textural properties of the catalysts were evaluated from N_2 adsorption–desorption isotherms (Fig. S23), and the results are listed in Table S8. The BET surface area of the fresh CMO-10 catalyst was considerably larger (185.3 m^2 g^{-1}) than that of the fresh CMO-0 catalyst (103.5 m^2 g^{-1}). The BET surface area of CMO-25 and CMO-50 increased to 214.1 and 210.5 m^2 g^{-1}, respectively. Thus, Mn suppressed interparticle agglomeration during calcination. Agglomeration between neighboring NPs during the reduction resulted in an increase in the particle size in the reduced CMO-0 catalyst (Fig. S24). The average particle diameter of the reduced CMO-0 catalyst increased significantly to 224 nm. In contrast, the Mn promoter suppressed the particle growth during reduction (Fig. S25); the average particle diameter in the reduced CMO-10 catalyst was an order of magnitude smaller (18.4 nm) than that in the reduced CMO-0 catalyst. Mn and Na species were distributed uniformly over the reduced CMO-10 catalyst. The Na contents in the reduced CMO-0 and CMO-10 catalysts were 0.11 and 0.12 wt%, respectively, as identified from the ICP–OES analysis (Table S9).

The overall morphology of the spent CMO-0 catalyst and its particle size did not change significantly compared to that of the reduced catalyst (Figs. S26A and B). A 10–15-nm-thick layer covered the outermost surface of the catalyst particles (Fig. S26C and E). Fast Fourier transform (FFT) and high-magnification images indicated the presence of diffraction patterns associated with CoO (111), Co_3O_4 (311), Co_2C (020), and hcp Co (012) and (101) planes in the spent CMO-0 catalyst, implying the formation of CoO_x and Co_2C phases during CO_2 hydrogenation (Figs. S26D and E). In the CoO_x/Co_2C layer, interlayer spacing was in the range of 2.44–2.56 Å, matching the lattice-expanded (311) plane of Co_3O_4 (2.44 Å) and (111) plane of CoO (2.46 Å) because of the presence of oxygen vacancies [39]. The HAADF–STEM images and their corresponding EDX images showed that oxygen and carbon species covered the surface of metallic Co particles (Figs. S26F–L). A close inspection of the EDX image of Co (Fig. S26M) revealed that a dense metallic Co phase in the core and a highly porous Co phase in the shell layer co-existed in the catalyst. The porous Co phase overlapped the O and C elements (Figs. S26N and O). Thus, an oxygen- and carbon-rich shell with a thickness of 10–15 nm formed on the surface of the metallic Co cores. At the outermost surface region, an approximately 5-nm-thick carbon layer was observed (Fig. S26O); this was formed by the FTS reaction. Thus, a carbon layer was deposited at the outermost surface of the spent CMO-0 catalyst, whereas CoO_x and Co_2C phases were present in close proximity at the subsurface region, resulting in a core-shell structured $Co@Co_2C/CoO_x$. However, in some part of the catalyst, the Co_2C/CoO_x shell layer was not uniform and carbon-rich phases detached from the catalyst surface were observed (Fig. S27).

The particle size of the spent CMO-10 catalyst increased to approximately 100 nm (Fig. 4A and B) compared to the reduced CMO-10 catalyst (18.4 nm, Fig. S25), indicating the occurrence of interparticle agglomeration during CO_2 hydrogenation. However, the particle size of the spent CMO-10 catalyst was much smaller compared to the spent CMO-0 catalyst, implying that the Mn promoter suppressed particle agglomeration during CO_2 hydrogenation. As in the case of the CMO-0 catalyst, the spent CMO-10 catalyst exhibited an hcp Co core and CoO_x/Co_2C shell structure (Fig. 4C–E). When considering the extremely small amount of Co oxides detected via the bulk analysis techniques (XRD and XAS, Fig. S7 and Fig. 3B, respectively) and the substantial amount of Co oxides detected via the surface-sensitive technique (XPS, Fig. S15B), the cobalt oxide species observed in the EDX images were predominantly present on the outermost surface of the metallic Co cores (Fig. 4M–O). The Mn promoter suppressed the formation of a carbon-rich layer on the outermost surface of the CMO-10 catalyst (Fig. 4O) and that of isolated carbon-rich sheets detached from the catalyst surface (Fig. S28). This resulted in the formation of a uniform CoO_x/Co_2C shell layer on individual Co core NPs.

The HR–TEM images of the spent CMO-0 and CMO-10 catalysts at varying reaction conditions were collected to further investigate the structural evolution at the surface of the catalyst and the effect of surface

structure on CO_2 hydrogenation performance. The thickness of shell layer in the spent CMO-0 catalyst collected after the 1.0 MPa reaction (C_1–C_4 selectivity = 98.3%, C_{5+} selectivity = 1.7%; Fig. 2A) was approximately 5 nm (Fig. S29); this was considerably thinner than that collected after the 4.0 MPa reaction (10–15 nm, Fig. S26E). Further, the surface layer of the spent CMO-0 catalyst at 1.0 MPa exhibited a higher $[CoO+Co_3O_4]/Co^0$ ratio (3.1) and lower carbide area% (3.0%) than that of the spent CMO-0 catalyst at 4.0 MPa (1.8% and 18.8%, respectively, Figs. S17D and E). The formation of small carbide species under low pressure was confirmed by comparing temperature-programmed hydrogenation–mass spectrometer (TPH–MS) profiles of the spent CMO-0 catalysts collected after reactions at 1.0 and 4.0 MPa (Fig. S30). The metallic Co content of the spent CMO-0 catalyst at 1.0 MPa was considerably lower (89.1%) than that at 4.0 MPa (98.6%, Table S5). In the case of the spent CMO-10 catalyst at 1.0 MPa (C_1–C_4 selectivity = 93.8%, C_{5+} selectivity = 6.2%; Fig. 2B), an evolution of the well-faceted, rectangular-shaped Co_2C particles with sizes of approximately 5 nm formed on the surface of the metallic Co particles (Fig. S31). This indicates that the formation of Co_2C was facilitated by the presence of the Mn promoter [40,41]. However, the formation of rectangular-shaped Co_2C particles did not increase the C_{5+} yields. Similar to the case of the CMO-0 catalyst, the spent CMO-10 catalyst at 1.0 MPa exhibited a higher $[CoO+Co_3O_4]/Co^0$ ratio (2.1), higher carbide area% (20.6%), and lower metallic Co content (83.5%) compared to the values of the spent CMO-10 catalyst under 4.0 MPa (1.7, 14.7%, and 99.0%, respectively; Table S5 and Figs. S17D and E). Therefore, the rich Co oxide and Co_2C phases in the catalysts formed at low pressures exhibited a detrimental effect on C_{5+} yields.

Rectangular-shaped Co_2C particles was formed (Fig. S32) at a low temperature of 230 °C (C_1 selectivity = 69.9%, C_{5+} selectivity = 5.1%; Fig. S5A). As the temperature increased to 250 °C (C_1 selectivity = 82.1%, C_{5+} selectivity = 9.9%; Fig. S5A), the rectangular morphology of Co_2C disappeared, whereas an approximately 4-nm-thick shell layer of mixed Co_2C and CoO_x covered the metallic Co cores. At 270 °C (C_1 selectivity = 44.2%, C_{5+} selectivity = 32.9%; Fig. S5A), the thickness of the shell layer increased (10–15 nm). A drastic morphological change was observed in the spent CMO-10 catalyst collected at 310 °C (C_1 selectivity = 89.3% and C_{5+} was not produced; Fig. S5A). Severe interparticle agglomeration between neighboring Co NPs at 310 °C could cause the detachment of the carbon-rich layer. A closer inspection revealed that carbon-rich sheets comprising small Co_2C phases detached from the surface of metallic Co particles (Fig. S33). Thus, some portions of the catalyst surface exposed to the water were formed as a byproduct, and these surfaces could re-oxidize the catalyst surface to form the Co_3O_4 phase in the bulk Co cores. The Co_3O_4 and CoO contents in the spent CMO-10 catalyst at 310 °C were considerably higher (37.8%) than those of the catalyst collected at 270 °C (1%, Table S5). Thus, the high CH_4 selectivity at the low reaction temperature originated from the incomplete development of mixed CoO_x and Co_2C shell layer. At high temperatures, the re-oxidation of the metallic Co phase caused by the agglomeration of $Co@CoO_x/Co_2C$ NPs was considered to be responsible for the high CH_4 selectivity. A similar correlation between the C_{5+} selectivity and the Co_2C/CoO_x shell layer was observed by changing the H_2/CO_2 ratios (Fig. S34). The incomplete conversion of Co oxides to metallic Co under the H_2-deficient condition and the re-oxidation of the metallic Co phase caused by particle aggregation under the H_2-sufficient condition make it difficult to establish the FTS regime. The spent CMO-10 catalyst maintained its morphology after 1425 h on the stream reaction (Fig. S35).

The H_2–TPR profiles were collected to understand the reduction properties of CMO-*y* catalysts with varying Mn contents (Fig. S36 and Table S10). The high-temperature peaks at 427–470 °C in the CMO-*y* catalysts ($10 \leq y \leq 75$) indicated that spinel-structured $Co_xMn_{3-x}O_4$ hindered the reducibility of the catalyst. Further, the reduction temperature of $Co_3O_4 \rightarrow$ CoO increased from 258 °C (CMO-0) to 345 °C (CMO-75) with an increase in Mn contents, indicating the suppression of

the reducibility of cobalt oxides in the presence of Mn.

CO$_2$–TPD, CO–TPD, and H$_2$–TPD analyses were conducted to investigate the adsorption strength of reactants on the surface of CMO-*y* catalysts. The presence of the Mn promoter increased the adsorption of CO$_2$ (Fig. S37 and Table S11) and CO (Fig. S38 and Table S12); however, it decreased the adsorption of H$_2$ (Fig. S39 and Table S13). Thus, the strong adsorption of CO and CO$_2$ and the weak adsorption of H$_2$ over the Mn-promoted catalyst can result in a high C/H surface coverage ratio; this can help increase the CO$_2$ conversion and C$_{5+}$ selectivity by increasing the FTS rate over methanation.

3.3. In situ operando DRIFT analysis

A series of in situ DRIFT experiments were conducted to examine the evolution of reaction intermediates over the CMO-0 and CMO-10 catalysts to gain insight into the reaction mechanism behind the formation of C$_{5+}$ hydrocarbons. DRIFTS spectra were collected during the pressurization of the DRIFT cell with CO$_2$ from 0.1 to 3.0 MPa that contained a pre-H$_2$ reduced CMO-0 catalyst at 350 °C to identify the intermediate species derived from the adsorption of CO$_2$ on the surface of the catalyst (Fig. S40A). The detailed peak assignments are listed in Table S14. The intensities of the infrared (IR) bands of gaseous CH$_4$ at 3015 and 1305 cm^{-1} [42] and the bending of =C–H group at 949 cm^{-1} [43] increased as the CO$_2$ flow time increased from 1 to 90 min. The formation of CH$_4$ over the reduced CMO-0 catalyst indicates that CO$_2$ methanation occurred because of the pre-adsorbed H$_2$ that remained after the reduction. A further increase in the CO$_2$ flow time to 170 min decreased the IR bands associated with CH$_4$ and =C–H owing to the gradual consumption of the pre-adsorbed H$_2$ on the catalyst surface. Small peaks appeared at 2200–2000 cm^{-1} for a 3 min CO$_2$ flow. The peaks at 2130 cm^{-1}, 2094 and 2078 cm^{-1}, and 2059 cm^{-1} are ascribed to linearly adsorbed CO on the Co^{2+} site ([Co^{2+}–(CO)]), partially reduced Co$^{\delta+}$ site ([Co$^{\delta+}$–(CO)]), and metallic Co site ([Co^0–(CO)]), respectively [44]. Peaks at 1933 and 1914 cm^{-1} can be assigned to be bridge-bonded CO on the metallic Co site ([Co$_{two-fold}$–(CO)]) [45]. Thus, in the reduced CMO-0 catalyst, completely reduced metallic Co^0, partially oxidized Co$^{\delta+}$ (1 < δ < 2), and Co$^{(2+)}$O centers coexist. The intensity of the [Co$^{\delta+}$–(CO)] peak is high, indicating that the CO adsorption on the oxygen vacant-Co oxide site is dominant. In the 1200–900 cm^{-1} region, bands at 1082 and 1051 cm^{-1} can be ascribed to the methoxy group [42]. The small peak at 1637 cm^{-1} corresponds to adsorbed water [9]. Evolution of the adsorbed CO, H$_2$O, and gaseous CH$_4$ indicates the activity of RWGS and methanation reactions over the CMO-0 catalyst. After a 170 min CO$_2$ flow, the pressure on the DRIFT cell increased to 3.0 MPa. Then, the temperature of the cell increased to 270 °C while maintaining the pressure of 3.0 MPa. The intensity of the IR spectrum at 270 °C and under 3.0 MPa was very similar to that at 50 °C and under 3.0 MPa.

The IR spectra were collected after the gas flow of the DRIFT cell was switched from CO$_2$ to H$_2$ at 270 °C and under 3.0 MPa (Fig. S40B). After a 40 min H$_2$ flow, the intensity of the IR bands associated with =C–H, methoxy, and adsorbed CO species decreased, whereas those associated with CH$_4$ increased. The evolution of gaseous CO (CO$_{gas}$) at 2110 and 2170 cm^{-1} [46] was observed when the H$_2$ flow time increased to 60 min. In addition, distinct peaks associated with reaction intermediates were observed in the region 1800–1200 cm^{-1}; peaks at 1508 and 1340 cm^{-1} could be attributed to the asymmetric and symmetric vibrations (ν_{as}(O–C–O) and ν_s(O–C–O), respectively) of the monodentate carbonate (m-CO$_3^{2-}$) [47–49]; the peaks at 1618, 1269, and 976 cm^{-1} could be ascribed to the ν(C=O), ν_{as}(O–C–O), and ν_s(O–C–O) of bidentate carbonate (b-CO$_3^{2-}$) [48,49]. Further, the peaks at 1652, 1436, 1222, and 1038 cm^{-1} could be assigned to the ν(C=O), ν_{as}(O–C–O), δ(O–H), and ν_s(O–C–O) of bicarbonate (HCO$_3^-$) [9,47–49], and those at 1577, 1374, and 1362 cm^{-1} to ν_{as}(O–C–O), δ(C–H), and ν_s(O–C–O) of formate (HCOO$^-$) [9]. The formation of CO$_2$-adsorbed species (m-CO$_3^{2-}$, b-CO$_3^{2-}$, HCO$_3^-$, and

HCOO$^-$) was progressively activated by increasing the partial pressure of H$_2$. The time-evolution intensity of the IR bands of m-CO$_3^{2-}$, HCOO$^-$, [Co$^{\delta+}$–(CO)], CO$_{gas}$, and CH$_4$ with a continuous flow of H$_2$ is illustrated in Fig. S40C. At the initial H$_2$ flow of approximately 30 min, the intensity of IR bands of m-CO$_3^{2-}$, HCOO$^-$, HCO$^-$, [Co$^{\delta+}$–(CO)], CO$_{gas}$, and CH$_4$ decreased because the H$_2$ partial pressure was not sufficiently high to induce a hydrogenation reaction while a continuous gas flow kept desorbing the surface adsorbed species and diluting gaseous products. As shown in the inset figure, a close inspection of the induction period revealed that the m-CO$_3^{2-}$ and HCOO$^-$ peaks had the minimum intensity at the initial 30 min H$_2$ flow, where those of CO$_{gas}$ and CH$_4$ were observed at the 40 min H$_2$ flow. Further, changes in the intensity of IR bands of m-CO$_3^{2-}$/HCOO$^-$, CO, and CH$_4$ are different; [Co$^{\delta+}$–(CO)] and CO$_{gas}$ reached their maximum intensity at the 90 min H$_2$ flow and decreased to almost zero with a further increase in the H$_2$ flow time. In contrast, the m-CO$_3^{2-}$ and HCOO$^-$ species reached their maximum intensity at 170 min and maintained their intensity with a further increase in the H$_2$ flow time. Different evolution trends of CO and m-CO$_3^2$/HCOO$^-$ suggest that the formation of m-CO$_3^{2-}$/HCOO$^-$ and CO follow different reaction pathways. The intensity of CH$_4$ increased for a time interval of 90–170 min where the IR band intensity of CO decreased; this suggests that CO is an intermediate for the formation of CH$_4$.

The behaviors of CO$_2$ adsorption over the CMO-10 catalyst exhibited a similar trend with the CMO-0 catalyst (Fig. 5). Unlike the previous Mn-promoted Co-based FTS catalysts [46,50], Mn in the Co catalyst did not red shift [Co^{2+}–(CO)], [Co$^{\delta+}$–(CO)], and ([Co^0–(CO)]) peaks, and it did not change the intensity of the [Co$_{two-fold}$–(CO)] peak. Therefore, in the CMO-10 catalyst, Mn played a minor role as an electronic promoter that changes the adsorption geometry of CO. During CO$_2$ adsorption, the intensities of the IR bands of gaseous CH$_4$ at 3015 and 1305 cm^{-1} and the bending of the =C–H group at 949 cm^{-1} reached their maximum values at 170 min (Fig. 5A); this is slower than those over the CMO-0 catalyst (90 min). This indicates that the Mn promotor suppressed methanation under the H$_2$-deficient condition. Again, decoupling in the evolution of m-CO$_3^{2-}$/HCOO$^-$ and CO$_{gas}$ at the H$_2$ flow time of 30–60 min indicates different reaction pathways in the formation of the formate and CO (Fig. 5C). Quadrupole mass spectrometry (QMS) profiles of products emitted from the DRIFT cell during the H$_2$ flow indicate the formation of CO and H$_2$O by the RWGS reaction, and that of CH$_4$, C$_2$H$_6$, and C$_3$H$_8$ by FTS over the CMO-10 catalyst (Fig. 5D).

DRIFTS spectra were collected by flowing CO with increasing pressures from 0.1 to 3.0 MPa in the DRIFTS cell that contained a pre-H$_2$ reduced CMO-0 catalyst at 350 °C to identify the intermediate species derived from the adsorption of CO on the surface of the catalyst (Fig. S41A). Unlike CO$_2$ adsorption, the formation of CH$_4$ was not observed during the CO adsorption, which indicates the direct CO hydrogenation to CH$_4$ did not occur under the H$_2$ deficient condition. Thus, the formation of CH$_4$ during the pressurization of CO$_2$ over the pre H$_2$-reduced CMO-0 catalyst (Fig. 5A) implies that the direct hydrogenation of CO$_2$ to CH$_4$ occurred without passing through CO, and the surface-adsorbed CO species did not participate in the methanation reaction under the H$_2$-deficient condition. CO$_2$ peaks at 2333 and 2364 cm^{-1} are prominent for the initial 15 min CO adsorptions (Fig. S41C), which indicates the high WGS activity of the CMO-0 catalyst. When the temperature increased from 50° to 270 °C, peaks associated with CO$_2$ increased because of the increased activity for the WGS reaction with increasing temperature [51]. After CO adsorption at 3.0 MPa, the gas flows through the DRIFT cell switched from CO to H$_2$ at 270 °C and under 3.0 MPa, and the IR spectra are collected (Fig. S41B). The spectra collected during the hydrogenation of the pre-adsorbed CO are similar to those of the hydrogenation of the pre-adsorbed CO$_2$ owing to the presence of in-situ produced CO$_2$ caused by the WGS reaction. The behaviors of CO adsorption and hydrogenation of the adsorbed CO over the CMO-10 catalyst are similar to those over the CMO-0 catalyst (Fig. S42). The major difference is the WGS activity; at the initial 5 min CO flow,
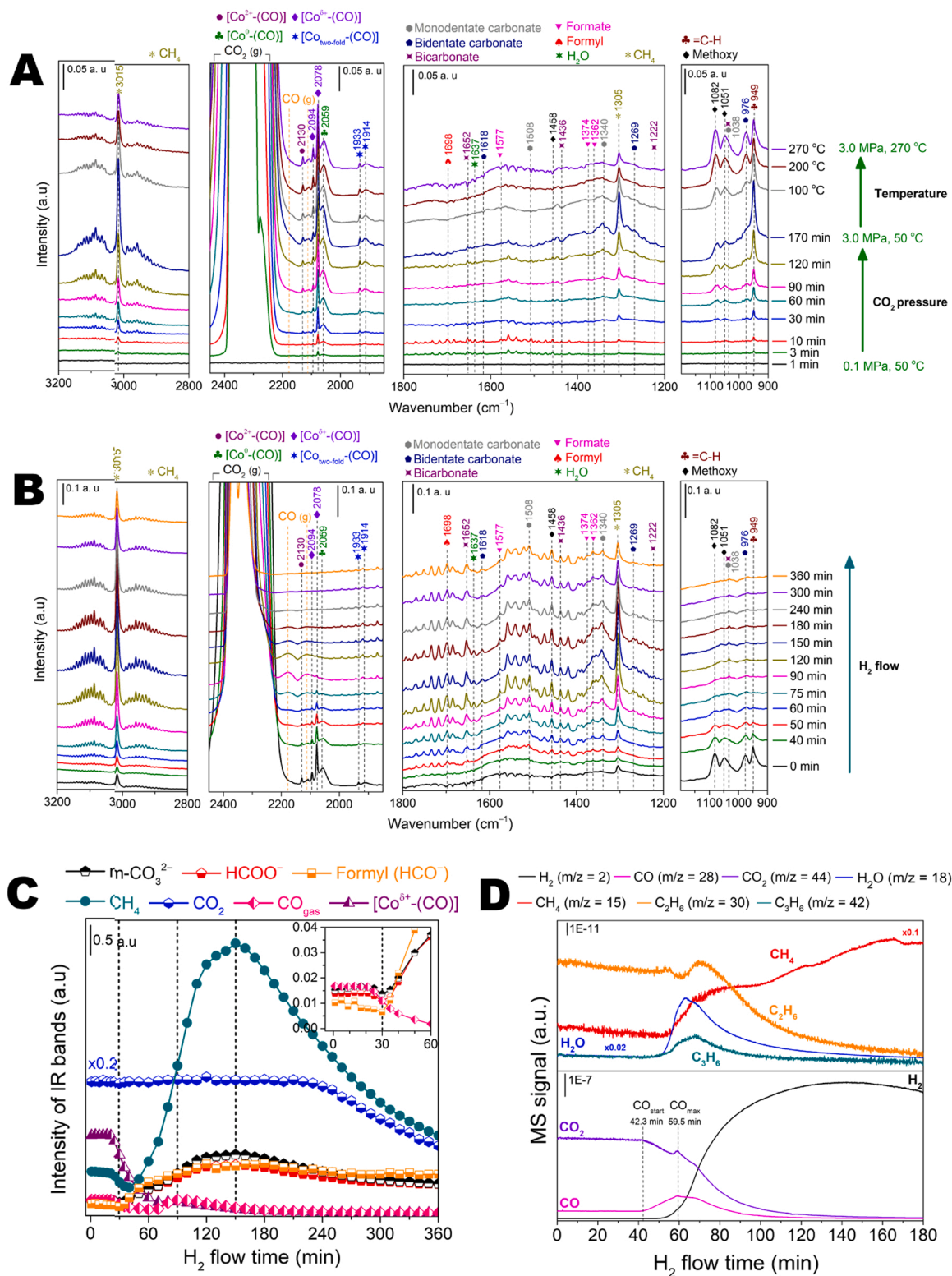
Fig. 5. In-situ DRIFT CO_2 adsorption profiles over the CMO-10 catalyst. (A) During the pressurization of the DRIFT cell using CO_2 to 3.0 MPa and the subsequent increment in temperature to 270 °C. (B) During the hydrogenation of CO_2-adsorbed species by switching the flow gas from CO_2 to H_2. (C) Evolution of selected CO_2-adsorbed species, CO, and CH_4 during hydrogenation. (D) QMS profiles of products emitted from the DRIFT cell under H_2 flow. Pretreatment conditions: Ramping rate = 2.5 °C min^{-1}, temperature = 350 °C, pressure = 3.0 MPa, H_2 flow rate = 50 mL min^{-1} for 6 h for the reduction, followed by purging with N_2 for 3 h; the cell was subsequently cooled to 50 °C. CO_2 adsorption conditions: CO_2 flow rate of 16.7 mL min^{-1} at 50 °C up to 3.0 MPa and increased temperature up to 270 °C. Hydrogenation conditions: Flow gas was switched from CO_2 to H_2 at a flow rate of 50 mL min^{-1}.

the intensity of gaseous CO_2 reached a maximum value over the CMO-10 catalyst, which is considerably faster than that over the CMO-0 catalyst. Both the gaseous CO_2 and CO were present at the end of the temperature ramping up to 270 °C at 3.0 MPa. At the early stage of the H_2 flow to the DRIFT cell that contains both the CO_2 and CO gases, the formation of H_2O by the RWGS over the CMO-10 catalyst is more prominent than those of the CMO-0 catalyst (Fig. S43). Therefore, the richer CO produced by RWGS over the CMO-10 catalyst facilitated the formation of C_2H_6, and subsequently CH_4, as the H_2 partial pressure increased compared to that over the CMO-0 catalyst.

In situ operando DRIFT profiles were collected under the flow of the H_2/CO_2 mixture with a ratio of 3:1 at 270 °C and under 3.0 MPa over the pre-H_2 reduced CMO-0 catalyst to examine the transient response of reaction intermediates during CO_2 hydrogenation. The collected DRIFT spectra and changes in the intensity of IR bands of the selected surface adsorbed species (m-CO_3^{2-}, HCOO$^-$, HCO$^-$, [Co$^{\delta+}$–(CO)]) and gases (CH_4, CO_2, CO) with time are shown in Fig. S44. After the induction period of 13 min, methanation was highly activated and peaks associated with m-CO_3^{2-}, HCOO$^-$, HCO$^-$, [Co$^{\delta+}$–(CO)], and CO_{gas} gradually increased. After 40 min H_2/CO_2 flow, the intensity of peaks associated with CO_{gas}, m-CO_3^{2-}, HCOO$^-$, and HCO$^-$ were maintained, whereas the intensity of the CH_4 peak decreased. Thus, after the consumption of the pre-adsorbed H_2 to produce CH_4, the ability of the CMO-0 catalyst for the dissociative adsorption of H_2 and subsequent hydrogenation of CO_2 to CH_4 was suppressed. After the 120 min H_2/CO_2 flow, the flow gas was switched from H_2/CO_2 to H_2, and the DRIFT spectra were collected (Fig. S44B). The CO_{gas} peak reached its maximum intensity at the 10 min H_2 flow, whereas the CH_4 and CO_2-adsorbed peaks reached their maximum intensity at the 70 min H_2 flow, which indicates activated methanation under the H_2-sufficient condition (Fig. S44C). Methanation was highly activated during the initial H_2/CO_2 flow over the CMO-10 catalyst, and this can be attributed to the smaller size metallic Co NPs compared to that over the CMO-0 catalyst (Fig. S45). Further, the

intensity of the peaks associated with m-CO_3^{2-} and HCOO$^-$ over the CMO-10 catalyst were higher than those over the CMO-0 catalyst during the CO_2/H_2 and subsequent H_2 flows, which indicate the enhanced CO_2 adsorption over the CMO-10 catalyst. A favorable formation of CO_2-adsorbed species as the pressure and temperature increased were observed in Figs. S46 and S47, respectively.

3.4. Density functional theory (DFT) simulation

The CMO-*y* catalyst is a mixture of metallic Co, Co carbide, and Co oxide phases, which can exchange reaction intermediates with each other, and therefore, it is challenging to identify their respective role in CO_2 conversion by decoupling each phase experimentally. To this end, the atomic-level mechanisms of the hydrogenation of CO_2 on the Co (001), Co_2C (101), and Co_3O_4 (110) surfaces were examined using DFT calculations. Although the CoO structure was observed in the HR–TEM image of the spent CMO-10 catalyst, DFT calculations found that the CoO slab was destabilized by the adsorbate (Table S15). Therefore, in this study, Co_3O_4 was selected as the representative structure of Co oxide and the mechanism was comparatively analyzed. Further, the effect of the surface oxygen vacancies of the Co_3O_4 phase (vac-Co_3O_4 (110)) on catalysis energetics was investigated. Fig. 6A and B show the CO_2 hydrogenation pathways and surface structures of the slabs, respectively. Since the hydrogenation and chain-growth reactions on various Co phases have been reported elsewhere [8,52–55], we focus on the energetics of the initial CO_2 activation and intermediates formations on the surfaces modeled in this study. The electronic formation energies, atomistic configurations, and frequencies of gaseous and adsorbed species are summarized in Table S15.

The initial CO_2 activation proceeds by forming three different intermediates of HCOO*, COOH*, and CO*. For the HCOO* pathway, the subsequent oxygen removal results in the formation of CH*, which serves as a precursor of FTS and methanation. As shown in Fig. 6C, the
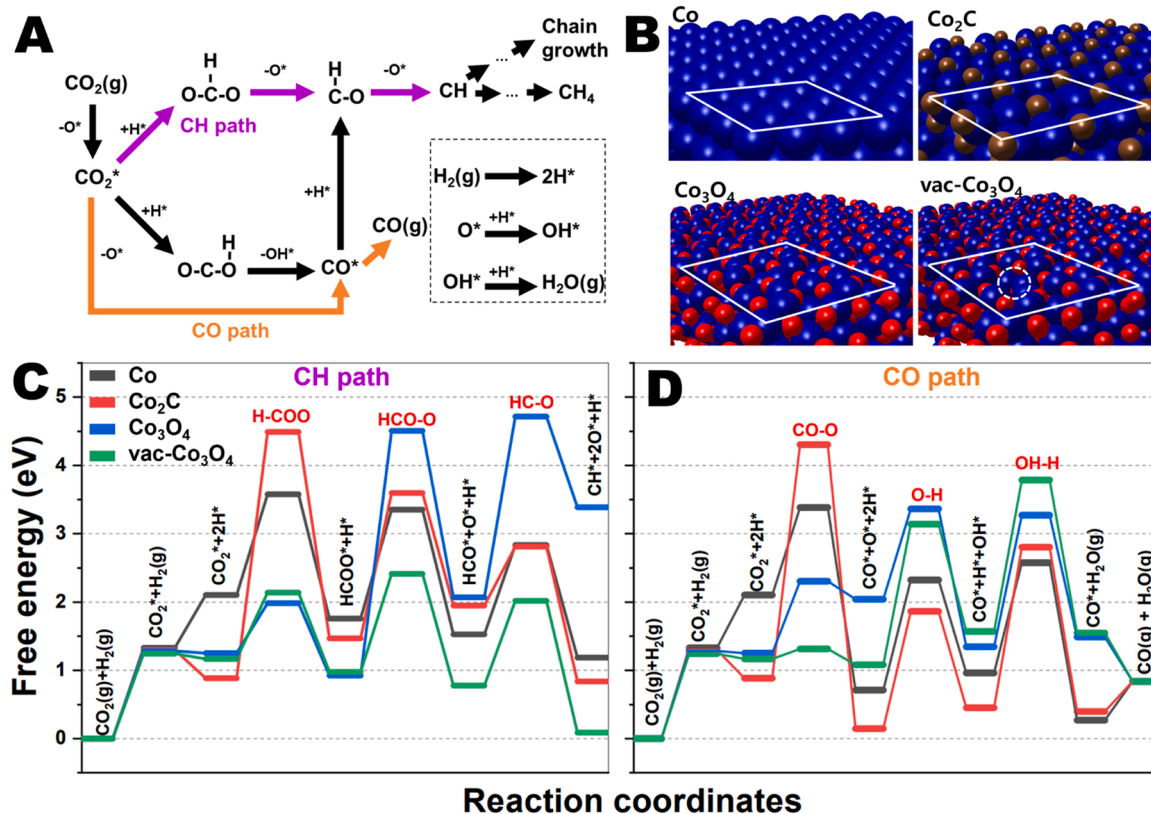

Fig. 6. (A) CO_2 hydrogenation pathways considered in this study. (B) Structures of Co (001), Co_2C (101), Co_3O_4 (110), vac-Co_3O_4 (110) surfaces. (C and D) Free energies of CO_2 hydrogenation for CH and CO under $T = 270$ °C and $P = 4.0$ MPa. * denotes surface-bound species.

formation of HCOO* (CO_2 * → H–COO → HCOO*) on the Co_3O_4 and vac-Co_3O_4 surfaces is favorable with small kinetic barriers of 0.73 and 0.97 eV, respectively. The subsequent oxygen removal of HCOO* for producing HCO* and CH* occurs on vac-Co_3O_4, whose kinetic barriers are considerably smaller than those on Co_3O_4. Therefore, the HCOO* - species shown in the DRIFT spectra (Fig. 5, Figs. S40–42, S46, S47) are present on the outmost Co oxide surfaces, and they can be readily converted to CHO* and CH* at adjacent oxygen defects. In addition to the CH* formation via the HCOO* pathway, Co oxide phases are active sites for proceeding with the RWGS reaction via the direct dissociation of OC–O bond (Fig. 6D). The activation of the OC–O bond scission on the vac-Co_3O_4 required only 0.15 eV. In contrast, the RWGS pathway via the HOCO* intermediate is not favorable because of the high activation barriers that occur regardless of the Co phases (Fig. S48B).

The free energy of CH* formation from gaseous CO is shown in Fig. S48C. Unlike the initial activation of CO_2, the CO adsorption and its successive hydrogenation are favorable on the Co_2C and metallic Co surfaces. The deoxygenation of CHO* to CH* on the Co_2C surface shows the activation energy of 0.86 eV, which is 0.4 eV lower than that on vac-Co_3O_4. Based on reaction energetics obtained using DFT simulation and DRIFT spectra, a plausible two-step reaction pathway for CO_2 hydrogenation to C_{5+} over the CMO catalyst was proposed; initially, CO_2 activation occurs at oxygen vacant sites of Co oxides in the shell, which produce CHO* and CO* intermediates. These intermediates then migrate to the nearby Co_2C and metallic Co at the core, where further hydrogenation or chain-growth reactions occur [8,52].

As discussed thus far, the high-yield C_{5+} over the CMO-0 and CMO-10 catalysts can be attributed to the activated FTS reaction on the hcp Co site. Further, the thermodynamic limitation of RWGS (e.g., approximately 18% CO_2 conversion at 270 °C and H_2/CO_2 ratio of 3) [56] can be overcome by facilitating subsequent CO consumption by the C–C coupling reaction over the metallic Co center. Besides low pressure (where the dominant methanation regime was observed), CO was barely detected in the stream of products during CO_2 hydrogenation. The evolutions of CO and CO_2 in the DRIFT profiles during CO_2 adsorption and CO_2 hydrogenation and in those during CO hydrogenation, respectively, indicate that the CMO-0 and CMO-10 catalysts are highly active in the both RWGS and WGS reactions. Thus, the negligible amount of CO in the product stream can be attributed to the swift conversion of CO over the hcp Co metal center. The conversion of CO_2 to CO via RWGS occurs on the porous CoO_x shell layer when considering the compositional geometry, electronic state of the spent CMO-0 and CMO-10 catalyst (core-shell Co@CoO_x/Co_2C), and DFT simulation. The surface oxygen vacant sites in the Co_3O_4 phase, which remained because of the incomplete transformation of Co_3O_4 to metallic Co during the reduction or were regenerated because of the water formed during the reaction, helped enhance CO_2 adsorption and RWGS reaction. Further, the sufficient production of CO by RWGS of CO_2 can help maintain the Co_2C shell layer via CO carburization ($2CoO + 4CO → Co_2C + 3CO_2$)

[57]. The produced CO was then transferred to the nearby Co_2C phase and metallic Co center in the core, where an active chain propagation reaction occurred (Fig. 7). The presence of the metallic Co center in the core and the CoO_x/Co_2C layers in the shell can affect the direct contact between CO_2 and the metallic Co phase; this effectively suppresses the direct CO_2 methanation reaction ($CO_2 + 4 H_2 → CH_4 + 2 H_2O$, ΔH^o (298 K) = −165 kJ mol^{-1}), which is a more favorable reaction than the RWGS reaction, thermodynamically ($CO_2 + H_2 → CO + H_2O$, ΔH^o (298 K) = 41 kJ mol^{-1}). The negligible formation of alcohols or other oxygenated species, which proceeds by the insertion of CO that adsorbed cobalt oxides [58] or Co_2C [59], were barely observed in the liquid products, which indicate CO insertion occurred negligibly over the CMO-0 and CMO-10 catalysts.

The Mn promotor significantly enhanced CO_2 conversion and C_{5+} selectivity in the CMO-10 catalyst. Further, the Mn promotor effectively suppressed particle aggregation during CO_2 hydrogenation, which could further enhance the CO_2 adsorption and RWGS reaction. However, as demonstrated in the CO and CO_2 DRIFT analyses, the IR band of the linearly adsorbed CO was not red shifted over the CMO-10 catalyst (which was also observed in the previous Mn-promoted Co/TiO_2 [46] and Co–Mn [50]); the considerably larger metallic Co size in the unsupported CMO-10 catalyst can minimize the effect of electron donation from $MnCO_3$ to metallic Co on the CO adsorption geometry. Mn facilitated the formation of the CoO_x/Co_2C shell layer, which further activated the RWGS reaction. The detachment of the CoO_x/Co_2C shell from the metallic Co center at the high temperature of 310 °C resulted in the re-oxidation of hcp Co and decrement in the FTS activity. Another characteristic of the CMO-10 catalyst in the FT-dominant regime is its ability to maintain a high metallic Co content. When the metallic Co center is an active site for a chain propagation reaction, it is necessary to suppress the re-oxidation of metallic Co caused by the direct contact of CO_2 or by H_2O produced from the RWGS reaction. For the FTS reaction, nano-sized Co particles (< 4–6 nm) are known to be highly susceptible for re-oxidation, which is attributed to their low FTS activity [60]. Thus, the high-yield C_{5+} over the CMO-10 catalyst indicates that moderate temperatures (270 °C) and high pressures (4.0 MPa) are beneficial for maintaining the metallic characteristic of Co in the core of the Co@CoO_x/Co_2C catalyst (Fig. 3F and G). The long-term catalytic stability, high selectivity toward gaseous/liquid fuels and lube base oil, and low-temperature synthetic condition make the Mn-promoted core-shell Co@CoO_x/Co_2C catalyst highly promising for unitization of CO_2 under industry-relevant conditions.

4. Conclusion

We demonstrated that a Mn-promoted core-shell Co@CoO_x/Co_2C catalyst produced liquid fuels and lube base oil in a one-pass CO_2 conversion. At a mild temperature of 270 °C, high-yield C_{5+} (21.1%) was achieved at a CO_2 conversion rate of 64.3%. As the time-on-stream
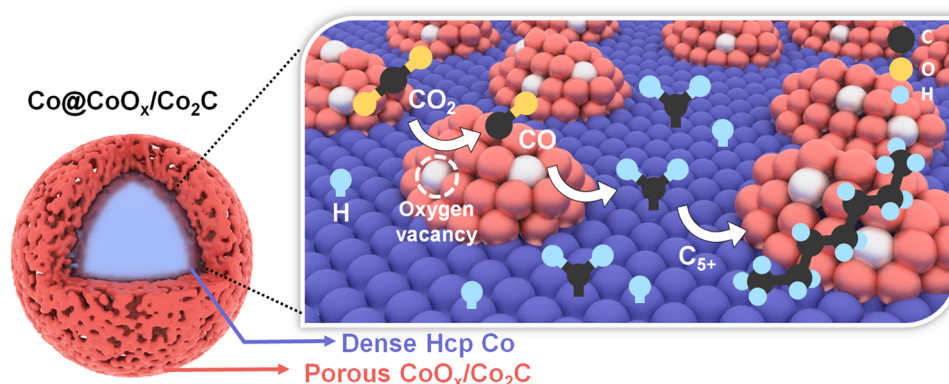

Fig. 7. Schematic for the reaction mechanism of the core-shell Co@CoO_x/Co_2C catalyst in the direct conversion of CO_2 to long-chain C_{5+} hydrocarbons.

increased to 1425 h, the C_{21+} selectivity increased to 14.9%. The oxygen-vacant CoO_x in the outmost shell layer activated the RWGS reaction, and the produced CO was transported to the nearby Co_2C phase and metallic Co center in the core, thereby producing long-chain C_{5+} via the FTS reaction. The metallic Co content was > 98% at the optimum reaction conditions (temperature of 270 °C, pressure of 4.0 MPa, H_2/CO_2 ratio of 3:1, and GHSV of 4000 mL g^{-1} h^{-1}) that could establish an FTS-dominant regime in the CO_2 hydrogenation; however, in the methanation-dominant regime (low pressures and high temperatures), the metallic Co content was 60%–90%. The long-term catalytic stability, high selectivity toward liquid fuels and lube base oil, and low-temperature synthetic condition make the Mn-promoted core-shell $Co@CoO_x$/Co_2C catalyst highly promising for unitization of CO_2 under industry-relevant conditions.

CRediT authorship contribution statement

Heuntae Jo: Conceptualization, Methodology, Formal analysis, Data curation, Writing – original draft. **Muhammad Kashif Khan:** Conceptualization, Methodology, Investigation. **Muhammad Irshad:** Validation, Data curation, Visualization. **Malik Waqar Arshad:** Methodology, Formal analysis, Investigation. **Seok Ki Kim:** Supervision, Resources, Writing – review & editing, Formal analysis, Investigation. **Jaehoon Kim:** Supervision, Project administration, Resources, Writing – review & editing, Funding acquisition.

Declaration of Competing Interest

The authors declare that they have no known competing financial interests or personal relationships that could have appeared to influence the work reported in this paper.

Acknowledgements

Appendix A. Supporting information

Supplementary data associated with this article can be found in the online version at doi:10.1016/j.apcatb.2021.121041.

References

[1] M.D. Porosoff, B. Yan, J.G. Chen, Catalytic reduction of CO_2 by H2 for synthesis of CO, methanol and hydrocarbons: challenges and opportunities, Energy Environ. Sci. 9 (2016) 62–73, https://doi.org/10.1039/C5EE02657A.

[2] M.G. Sibi, M.K. Khan, D. Verma, W. Yoon, J. Kim, High-yield synthesis of BTEX over Na–FeAlOx/Zn–HZSM-5@SiO2 by direct CO_2 conversion and identification of surface intermediates, Appl. Catal. B 301 (2022), 120813, https://doi.org/10.1016/j.apcatb.2021.120813.

[3] M.G. Sibi, D. Verma, H.C. Setiyadi, M.K. Khan, N. Karanwal, S.K. Kwak, K. Y. Chung, J.-H. Park, D. Han, K.-W. Nam, J. Kim, Synthesis of monocarboxylic acids via direct CO_2 conversion over Ni–Zn intermetallic catalysts, ACS Catal. 11 (2021) 8382–8398, https://doi.org/10.1021/acscatal.1c00747.

[4] S. Zhang, Z. Wu, X. Liu, Z. Shao, L. Xia, L. Zhong, H. Wang, Y. Sun, Tuning the interaction between Na and Co2C to promote selective CO_2 hydrogenation to ethanol, Appl. Catal. B 293 (2021), 120207, https://doi.org/10.1016/j.apcatb.2021.120207.

[5] M.K. Gnanamani, W.D. Shafer, D.E. Sparks, B.H. Davis, Fischer–Tropsch synthesis: effect of CO_2 containing syngas over Pt promoted Co/γ-Al2O3 and K-promoted Fe catalysts, Catal. Commun. 12 (2011) 936–939, https://doi.org/10.1016/j.catcom.2011.03.002.

[6] Q. Yang, A. Skrypnik, A. Matvienko, H. Lund, M. Holena, E.V. Kondratenko, Revealing property-performance relationships for efficient CO_2 hydrogenation to higher hydrocarbons over Fe-based catalysts: statistical analysis of literature data

[7] A.Y. Khodakov, W. Chu, P. Fongarland, Advances in the development of novel cobalt Fischer−Tropsch catalysts for synthesis of long-chain hydrocarbons and clean fuels, Chem. Rev. 107 (2007) 1692–1744, https://doi.org/10.1021/cr050972v.

[8] L. Zhong, F. Yu, Y. An, Y. Zhao, Y. Sun, Z. Li, T. Lin, Y. Lin, X. Qi, Y. Dai, L. Gu, J. Hu, S. Jin, Q. Shen, H. Wang, Cobalt carbide nanoprisms for direct production of lower olefins from syngas, Nature 538 (2016) 84–87, https://doi.org/10.1038/nature19786.

[9] C.G. Visconti, L. Lietti, E. Tronconi, P. Forzatti, R. Zennaro, E. Finocchio, Fischer–Tropsch synthesis on a Co/Al2O3 catalyst with CO_2 containing syngas, Appl. Catal. A 355 (2009) 61–68, https://doi.org/10.1016/j.apcata.2008.11.027.

[10] S. Saeidi, N.A.S. Amin, M.R. Rahimpour, Hydrogenation of CO_2 to value-added products—a review and potential future developments, J. CO2 Util. 5 (2014) 66–81, https://doi.org/10.1016/j.jcou.2013.12.005.

[11] K.Y. Kim, H. Lee, W.Y. Noh, J. Shin, S.J. Han, S.K. Kim, K. An, J.S. Lee, Cobalt ferrite nanoparticles to form a catalytic Co–Fe alloy carbide phase for selective CO_2 hydrogenation to light olefins, ACS Catal. 10 (2020) 8660–8671, https://doi.org/10.1021/acscatal.0c01417.

[12] L. Wang, S. He, L. Wang, Y. Lei, X. Meng, F.-S. Xiao, Cobalt–nickel catalysts for selective hydrogenation of carbon dioxide into ethanol, ACS Catal. 9 (2019) 11335–11340, https://doi.org/10.1021/acscatal.9b04187.

[13] R.W. Dorner, D.R. Hardy, F.W. Williams, H.D. Willauer, Heterogeneous catalytic CO_2 conversion to value-added hydrocarbons, Energy Environ. Sci. 3 (2010) 884–890, https://doi.org/10.1039/C001514H.

[14] M.K. Khan, P. Butolia, H. Jo, M. Irshad, D. Han, K.-W. Nam, J. Kim, Selective conversion of carbon dioxide into liquid hydrocarbons and long-chain α-olefins over Fe-amorphous AlOx bifunctional catalysts, ACS Catal. 10 (2020) 10325–10338, https://doi.org/10.1021/acscatal.0c02611.

[15] R.F. Susanti, L.W. Dianningrum, T. Yum, Y. Kim, B.G. Lee, J. Kim, High-yield hydrogen production from glucose by supercritical water gasification without added catalyst, Int. J. Hydrog. Energy 37 (2012) 11677–11690, https://doi.org/10.1016/j.ijhydene.2012.05.087.

[16] M.K. Khan, R. Insyani, J. Lee, M. Yi, J.W. Lee, J. Kim, A non-catalytic, supercritical methanol route for effective deacidification of naphthenic acids, Fuel 182 (2016) 650–659, https://doi.org/10.1016/j.fuel.2016.06.023.

[17] G. Kresse, J. Furthmüller, Efficient iterative schemes for ab initio total-energy calculations using a plane-wave basis set, Phys. Rev. B 54 (1996) 11169–11186, https://doi.org/10.1103/PhysRevB.54.11169.

[18] K. Lee, É.D. Murray, L. Kong, B.I. Lundqvist, D.C. Langreth, Higher-accuracy van der Waals density functional, Phys. Rev. B 82 (2010), 081101, https://doi.org/10.1103/PhysRevB.82.081101.

[19] R. Zhang, G. Wen, H. Adidharma, A.G. Russell, B. Wang, M. Radosz, M. Fan, C2 oxygenate synthesis via Fischer–Tropsch synthesis on Co2C and Co/Co2C interface catalysts: how to control the catalyst crystal facet for optimal selectivity, ACS Catal. 7 (2017) 8285–8295, https://doi.org/10.1021/acscatal.7b02800.

[20] X.L. Xu, J.Q. Li, DFT studies on H2O adsorption and its effect on CO oxidation over spinel Co3O4 (110) surface, Surf. Sci. 605 (2011) 1962–1967, https://doi.org/10.1016/j.susc.2011.07.013.

[21] B.S. Youmbi, F. Calvayrac, Structure of CoO(001) surface from DFT+U calculations, Surf. Sci. 621 (2014) 1–6, https://doi.org/10.1016/j.susc.2013.10.012.

[22] G. Yan, P. Sautet, Surface structure of Co3O4 (111) under reactive gas-phase environments, ACS Catal. 9 (2019) 6380–6392, https://doi.org/10.1021/acscatal.9b01485.

[23] C.J. Cramer, Essentials of Computational Chemistry: Theories and Models, John Wiley & Sons, 2013.

[24] J.A. Garrido Torres, P.C. Jennings, M.H. Hansen, J.R. Boes, T. Bligaard, Low-scaling algorithm for nudged elastic band calculations using a surrogate machine learning model, Phys. Rev. Lett. 122 (2019), 156001, https://doi.org/10.1103/PhysRevLett.122.156001.

[25] S. Rößler, C. Kern, A. Jess, Accumulation of liquid hydrocarbons during cobalt-catalyzed Fischer–Tropsch synthesis - influence of activity and chain growth probability, Catal. Sci. Technol. 9 (2019) 4047–4054, https://doi.org/10.1039/C9CY00671K.

[26] J. Wei, Q. Ge, R. Yao, Z. Wen, C. Fang, L. Guo, H. Xu, J. Sun, Directly converting CO_2 into a gasoline fuel, Nat. Commun. 8 (2017) 15174, https://doi.org/10.1038/ncomms15174.

[27] A. Ramirez, A. Dutta Chowdhury, A. Dokania, P. Cnudde, M. Caglayan, I. Yarulina, E. Abou-Hamad, L. Gevers, S. Ould-Chikh, K. De Wispelaere, V. van Speybroeck, J. Gascon, Effect of zeolite topology and reactor configuration on the direct conversion of CO_2 to light olefins and aromatics, ACS Catal. 9 (2019) 6320–6334, https://doi.org/10.1021/acscatal.9b01466.

[28] X. Cui, P. Gao, S. Li, C. Yang, Z. Liu, H. Wang, L. Zhong, Y. Sun, Selective production of aromatics directly from carbon dioxide hydrogenation, ACS Catal. 9 (2019) 3866–3876, https://doi.org/10.1021/acscatal.9b00640.

[29] Ad Klerk, Fischer–Tropsch fuels refinery design, Energy Environ. Sci. 4 (2011) 1177–1205, https://doi.org/10.1039/C0EE00692K.

[30] L. Guo, Y. Cui, P. Zhang, X. Peng, Y. Yoneyama, G. Yang, N. Tsubaki, Enhanced liquid fuel production from CO_2 Hydrogenation: catalytic performance of bimetallic catalysts over a two-stage reactor system, ChemistrySelect 3 (2018) 13705–13711, https://doi.org/10.1002/slct.201803335.

[31] A. Bordet, J.M. Asensio, K. Soulantica, B. Chaudret, Enhancement of carbon oxides hydrogenation on iron-based nanoparticles by in-situ water removal, ChemCatChem 10 (2018) 4047–4051, https://doi.org/10.1002/cctc.201800821.

[32] A. Dinse, M. Aigner, M. Ulbrich, G.R. Johnson, A.T. Bell, Effects of Mn promotion on the activity and selectivity of Co/SiO2 for Fischer–Tropsch synthesis, J. Catal. 288 (2012) 104–114, https://doi.org/10.1016/j.jcat.2012.01.008.

[33] W. Chen, I.A.W. Filot, R. Pestman, E.J.M. Hensen, Mechanism of cobalt-catalyzed CO hydrogenation: 2. Fischer–Tropsch synthesis, ACS Catal. 7 (2017) 8061–8071, https://doi.org/10.1021/acscatal.7b02758.

[34] W. Chen, T.F. Kimpel, Y. Song, F.-K. Chiang, B. Zijlstra, R. Pestman, P. Wang, E.J. M. Hensen, Influence of carbon deposits on the cobalt-catalyzed Fischer–Tropsch reaction: evidence of a two-site reaction model, ACS Catal. 8 (2018) 1580–1590, https://doi.org/10.1021/acscatal.7b03639.

[35] J.L. Martin de Vidales, E. Vila, R.M. Rojas, O. Garcia-Martinez, Thermal behavior in air and reactivity in acid medium of cobalt manganese spinels MnxCo3-xO4 (1. ltoreq. x.ltoreq. 3) synthesized at low temperature, Chem. Mater. 7 (1995) 1716–1721, https://doi.org/10.1021/cm00057a022.

[36] Z. Zhao, W. Lu, R. Yang, H. Zhu, W. Dong, F. Sun, Z. Jiang, Y. Lyu, T. Liu, H. Du, Y. Ding, Insight into the formation of Co@Co2C catalysts for direct synthesis of higher alcohols and olefins from syngas, ACS Catal. 8 (2018) 228–241, https://doi.org/10.1021/acscatal.7b02403.

[37] C.H. Wu, B. Eren, H. Bluhm, M.B. Salmeron, Ambient-pressure X-ray photoelectron spectroscopy study of cobalt foil model catalyst under CO, H2, and their mixtures, ACS Catal. 7 (2017) 1150–1157, https://doi.org/10.1021/acscatal.6b02835.

[38] Y. Zhu, X. Pan, F. Jiao, J. Li, J. Yang, M. Ding, Y. Han, Z. Liu, X. Bao, Role of manganese oxide in syngas conversion to light olefins, ACS Catal. 7 (2017) 2800–2804, https://doi.org/10.1021/acscatal.7b00221.

[39] X.-D. Zhou, W. Huebner, Size-induced lattice relaxation in CeO2 nanoparticles, Appl. Phys. Lett. 79 (2001) 3512–3514, https://doi.org/10.1063/1.1419235.

[40] T. Lin, K. Gong, C. Wang, Y. An, X. Wang, X. Qi, S. Li, Y. Lu, L. Zhong, Y. Sun, Fischer–Tropsch synthesis to olefins: catalytic performance and structure evolution of Co2C-based catalysts under a CO2 environment, ACS Catal. 9 (2019) 9554–9567, https://doi.org/10.1021/acscatal.9b02513.

[41] J. Paterson, M. Peacock, R. Purves, R. Partington, K. Sullivan, G. Sunley, J. Wilson, Manipulation of Fischer-Tropsch synthesis for production of higher alcohols using manganese promoters, ChemCatChem 10 (2018) 5154–5163, https://doi.org/10.1002/cctc.201800883.

[42] V. Sanchez-Escribano, M.A. Larrubia Vargas, E. Finocchio, G. Busca, On the mechanisms and the selectivity determining steps in syngas conversion over supported metal catalysts: an IR study, Appl. Catal. A 316 (2007) 68–74, https://doi.org/10.1016/j.apcata.2006.09.020.

[43] G.M.L.D.L. Pavia, G.S. Kriz, J.R. Vyvyan. Introduction to Spectroscopy, fifth ed., Cengage Learning, Stamford, CT, 2015.

[44] M. Jiang, N. Koizumi, T. Ozaki, M. Yamada, Adsorption properties of cobalt and cobalt-manganese catalysts studied by in situ diffuse reflectance FTIR using CO and CO+H2 as probes, Appl. Catal. A 209 (2001) 59–70, https://doi.org/10.1016/S0926-860X(00)00755-9.

[45] C.J. Weststrate, J. van de Loosdrecht, J.W. Niemantsverdriet, Spectroscopic insights into cobalt-catalyzed Fischer-Tropsch synthesis: a review of the carbon monoxide interaction with single crystalline surfaces of cobalt, J. Catal. 342 (2016) 1–16, https://doi.org/10.1016/j.jcat.2016.07.010.

[46] F. Morales, E. de Smit, F.M.F. de Groot, T. Visser, B.M. Weckhuysen, Effects of manganese oxide promoter on the CO and H2 adsorption properties of titania-

supported cobalt Fischer–Tropsch catalysts, J. Catal. 246 (2007) 91–99, https://doi.org/10.1016/j.jcat.2006.11.014.

[47] T. Das, G. Deo, Synthesis, characterization and in situ DRIFTS during the CO2 hydrogenation reaction over supported cobalt catalysts, J. Mol. Catal. A Chem. 350 (2011) 75–82, https://doi.org/10.1016/j.molcata.2011.09.008.

[48] L. Lukashuk, N. Yigit, R. Rameshan, E. Kolar, D. Teschner, M. Hävecker, A. Knop-Gericke, R. Schlögl, K. Föttinger, G. Rupprechter, Operando insights into CO oxidation on cobalt oxide catalysts by NAP-XPS, FTIR, and XRD, ACS Catal. 8 (2018) 8630–8641, https://doi.org/10.1021/acscatal.8b01237.

[49] A. Davydov, Molecular Spectroscopy of Oxide Catalyst Surfaces, John Wiley & Son Ltd., The Atrium, Southern Gate, Chichester, England, 2003.

[50] G.R. Johnson, S. Werner, A.T. Bell, An Investigation into the effects of Mn promotion on the activity and selectivity of Co/SiO2 for Fischer–Tropsch synthesis: evidence for enhanced CO adsorption and dissociation, ACS Catal. 5 (2015) 5888–5903, https://doi.org/10.1021/acscatal.5b01578.

[51] L. Gradisher, B. Dutcher, M. Fan, Catalytic hydrogen production from fossil fuels via the water gas shift reaction, Appl. Energy 139 (2015) 335–349, https://doi.org/10.1016/j.apenergy.2014.10.080.

[52] Z. Yao, C. Guo, Y. Mao, P. Hu, Quantitative determination of C–C coupling mechanisms and detailed analyses on the activity and selectivity for Fischer–Tropsch synthesis on Co(0001): microkinetic modeling with coverage effects, ACS Catal. 9 (2019) 5957–5973, https://doi.org/10.1021/acscatal.9b01150.

[53] B. Liu, W. Li, Y. Xu, Q. Lin, F. Jiang, X. Liu, Insight into the intrinsic active site for selective production of light olefins in cobalt-catalyzed Fischer–Tropsch synthesis, ACS Catal. 9 (2019) 7073–7089, https://doi.org/10.1021/acscatal.9b00352.

[54] J.-X. Liu, H.-Y. Su, D.-P. Sun, B.-Y. Zhang, W.-X. Li, Crystallographic dependence of CO activation on cobalt catalysts: HCP versus FCC, J. Am. Chem. Soc. 135 (2013) 16284–16287, https://doi.org/10.1021/ja408521w.

[55] M. Yu, L. Liu, Q. Wang, L. Jia, J. Wang, D. Li, B. Hou, Rediscovering tuning product selectivity by an energy descriptor: CH4 formation and C1–C1 coupling on the FCC Co surface, J. Phys. Chem. C 124 (2020) 11040–11049, https://doi.org/10.1021/acs.jpcc.0c02537.

[56] U. Rodemerck, M. Holeňa, E. Wagner, Q. Smejkal, A. Barkschat, M. Baerns, Catalyst development for CO2 hydrogenation to fuels, ChemCatChem 5 (2013) 1948–1955, https://doi.org/10.1002/cctc.201200879.

[57] J.C. Mohandas, M.K. Gnanamani, G. Jacobs, W. Ma, Y. Ji, S. Khalid, B.H. Davis, Fischer–Tropsch synthesis: characterization and reaction testing of cobalt carbide, ACS Catal. 1 (2011) 1581–1588, https://doi.org/10.1021/cs200236q.

[58] M. Blanchard, H. Derule, P. Canesson, Cobalt catalysts for the production of alcohols in the F.T. synthesis, Catal. Lett. 2 (1989) 319–322, https://doi.org/10.1007/BF00770230.

[59] M.K. Gnanamani, G. Jacobs, R.A. Keogh, W.D. Shafer, D.E. Sparks, S.D. Hopps, G. A. Thomas, B.H. Davis, Fischer-Tropsch synthesis: effect of pretreatment conditions of cobalt on activity and selectivity for hydrogenation of carbon dioxide, Appl. Catal. A 499 (2015) 39–46, https://doi.org/10.1016/j.apcata.2015.03.046.

[60] N.E. Tsakoumis, J.C. Walmsley, M. Rønning, W. van Beek, E. Rytter, A. Holmen, Evaluation of reoxidation thresholds for γ-Al2O3-supported cobalt catalysts under Fischer–Tropsch synthesis conditions, J. Am. Chem. Soc. 139 (2017) 3706–3715, https://doi.org/10.1021/jacs.6b11872.